Nationaal Lucht- en Ruimtevaartlaboratorium
National Aerospace Laboratory NLR

NLR-TP-98239

Space-time discontinuous Galerkin finite element method with dynamic grid motion for inviscid compressible flows

J.J.W. van der Vegt

Nationaal Lucht- en Ruimtevaartlaboratorium
National Aerospace Laboratory NLR

NLR-TP-98239

Space-time discontinuous Galerkin finite element method with dynamic grid motion for inviscid compressible flows

J.J.W. van der Vegt

This investigation has been carried out under a contract awarded by the Netherlands Agency for Aerospace Programmes (NIVR), contract number 07601N.
NIVR has granted NLR permission to publish this report.

This report is based on an article to be published in the Journal of Computational Physics, by the Academic Press.

Division:	Fluid Dynamics
Issued:	July 1998
Classification of title:	unclassified

Running head: Space-Time Discontinuous Galerkin Finite Element Method

Send proofs to:
Dr. J.J.W. van der Vegt
National Aerospace Laboratory NLR
Theoretical Aerodynamics Department
P.O. Box 90502, 1006BM Amsterdam
The Netherlands
Phone: +31 20 5113697
Fax: +31 20 5113210
E-mail: vegt@ nlr.nl

Abstract

A new space-time discontinuous Galerkin finite element method with dynamic grid motion for the solution of the Euler equations of gas dynamics is presented. The discontinuous Galerkin discretization presented in this paper results in an efficient upwind finite element method, which satisfies the Geometric Conservation Law, and provides an algorithm which requires significantly less flux calculations than discontinuous Galerkin discretizations using Gauss quadrature rules for the flux integrations. In addition, a less general but more efficient, discontinuous Galerkin discretization using a translating-rotating reference frame is discussed. This method is especially suited for problems with solid body rotation, but without grid deformation. An efficient implicit time integration method is discussed, where the non-linear equations of the implicit discretization are solved with a full approximation storage multigrid scheme. The formulation of a multigrid algorithm for both discontinuous Galerkin methods receives special attention. Simulations of a delta wing in pitching oscillation are used to demonstrate the numerical algorithms.

1 Introduction

This paper presents a new space-time Discontinuous Galerkin (DG) finite element method for the calculation of unsteady compressible flows in time-dependent flow domains. The main objective is to present a new discretization technique for time-accurate flow calculations on meshes with dynamic grid motion. In addition, a more specialized discretization technique is presented for the calculation of unsteady flows using a translating-rotating reference frame. This method is especially suited for problems with solid body rotation, but without grid deformation. This paper is the second paper in a sequel on the discontinuous Galerkin finite element method for compressible flows. The first paper, Van der Vegt and Van der Ven [25], discusses the solution of the three-dimensional steady Euler equations of gas dynamics with the discontinuous Galerkin finite element method. Special emphasis was put on the development of an anisotropic grid adaptation algorithm, with local grid refinement and coarsening, and the data structures required for efficient calculations on grids when elements are added and deleted during the adaptation process. Grid adaptation with local refinement and coarsening combines very well with the DG finite element method because it is a very local scheme, which does not require much grid smoothness. Grid adaptation is also very important for time-dependent flows, because important flow features generally move through the flow domain and need to be captured by the grid, but this paper concentrates on a general formulation of the DG finite element method suitable for moving and deforming flow domains without grid adaptation.

Unsteady flow calculations with moving bodies are of great practical importance in aerospace and many related fields and still present a great challenge to Computational Fluid Dynamics (CFD). Apart from the large computational effort required for this type of calculations there are also many algorithmic issues which need to be solved. Several new problems arise when grids are experiencing dynamic grid motion with moving boundaries, with as most important one satisfying the Geometric Conservation Law (GCL). The GCL states that a uniform flow field should not be influenced by dynamic grid motion, see Thomas and Lombard [21]. This is a non-trivial condition which imposes significant restrictions on discretization techniques and recently has received considerable attention, [12, 16, 29]. Other important problems are related to efficient time-integration methods, maintaining time-accuracy and obtaining an accurate fluid structure coupling.

The use of the discontinuous Galerkin finite element method for solving the Euler equations in time-dependent flow domains is motivated by some very useful properties of this method. The

DG finite element method uses polynomial expansions in each individual element without requiring continuity across element faces. In addition to the equations for the mean flow quantities separate equations for the flow gradients are solved. The DG method therefore does not require a reconstruction algorithm using data in neighboring elements to achieve second-order accuracy. The discontinuity in the polynomial expansions at element faces is represented as a Riemann problem and upwinding is introduced into the DG finite element method by using (approximate) Riemann solvers for the flux at element faces. The DG finite element method is a very local scheme, where the only connection with neighboring elements occurs in the solution of the Riemann problem at element faces and in the slope limiting procedure. The fact that the DG finite element discretization results in a very local, compact scheme makes it possible to maintain accuracy on highly irregular grids, such as those obtained by grid adaptation and was one of the main reasons for choosing this method. The DG discretization in time results in improved time accuracy in comparison with multi-step methods, as demonstrated by Eriksson and Johnson [7], and requires only the storage of one time level to achieve second-order accuracy.

The discontinuous Galerkin method with discontinuity in space, combined with a TVD Runge-Kutta time integration method, is analyzed in detail by Cockburn, Shu et al. [3, 4, 5]. The application to the solution of the three-dimensional Euler equations in combination with grid adaptation and an improved flux calculation method is presented by Van der Vegt and Van der Ven [23, 24, 25]. The discontinuous Galerkin method with discontinuity in time, but continuous in space, is discussed in a series of papers by Hansbo, Johnson et al. [9] and Shakib, Hughes et al. [18], and the references therein, in combination with the Streamline Upwind Petrov Galerkin (SUPG) method and its derivatives.

This paper discusses the discontinuous Galerkin method with discontinuous expansions both in space and time, because it provides the optimal flexibility in deriving numerical algorithms for problems with moving boundaries and dynamic grid motion. A major difference with the SUPG method is that these methods use specially constructed least-squares and discontinuity capturing operators, whereas the DG discretization presented in this paper automatically results in an upwind finite element method by solving the Riemann problems at the cell faces, which gives a close coupling with compressible flow physics. The main emphasis in this paper is on the formulation and efficient discretization of the space-time DG method, with special attention paid to an efficient calculation of the fluxes. The data locality of the DG finite element method makes it also a very good algorithm for parallel calculations, as was demonstrated by Van der Ven and Van der Vegt [26].

The efficient calculation of unsteady flows frequently requires an implicit time integration method due to the large disparity between the physically relevant time scales and those imposed by the stability constraints of explicit methods. In this paper a multigrid procedure is used to obtain an efficient implicit time integration method. This method was originally proposed by Jameson [11] and improved by Melson et al. [14] and has become very popular. The main benefits are that the method does not have the large storage requirements of conventional implicit schemes and fits well into the multigrid framework build for steady flow calculations. The full approximation storage multigrid algorithm for the solution of the non-linear equations of the implicit time integration method is also used in this paper. The formulation of a multigrid algorithm for the DG finite element method will receive special attention, because it requires a slightly different approach than the commonly used techniques in finite volume methods.

The DG finite element method is demonstrated with calculations of dynamic motion of a delta wing with a sharp leading edge in pitching oscillation. This is an important problem for aircraft maneuver and also relevant to aeroelasticity. The space-time DG finite element method and the DG discretization using a translating-rotating reference frame are compared, with special attention paid to the requirements for time-accuracy. This comparison serves both as a verification of both methods and to investigate the added cost of the more general space-time formulation. In order to investigate the capability of both methods to simulate unsteady vortical flow also a comparison is made with experiments from Löser [13].

The outline of the paper is as follows. First the algorithms for the space-time DG finite element method and the DG finite element method using a moving reference frame are discussed. After the presentation of the weak formulations for both methods the efficient calculation of the fluxes is discussed in detail. The approximations to the flux integrals result in a second-order accurate scheme, which does not require more flux calculations than required for second-order accurate finite volume methods. This is a significant improvement in efficiency compared to DG finite element methods using Gauss quadrature rules, as was originally proposed by Cockburn, Shu et al. [3, 4, 5]. Next, the implicit time integration method and some aspects of the multigrid scheme are discussed. The paper concludes with results of simulations of a delta wing in pitching oscillation, which are used to demonstrate both methods. The Appendix summarizes some important results for the calculation of the geometrical contributions in the flux calculation. The use of these relations automatically guarantees that the Geometric Conservation Law is satisfied because the geometric contributions then are calculated exactly.

2 Euler Equations in a Moving Domain

Let $\Omega(t) \subset R^3$ be a flow domain at time t. The relation between the flow domain at time t and initial time t_0 is described by the mapping:

$$\Phi : \tilde{\mathbf{x}} \in \Omega(t_0) \rightarrow \mathbf{x}(t) = \Phi(\tilde{\mathbf{x}}, t) \in \Omega(t). \tag{1}$$

The Jacobian J_Φ of the mapping Φ must satisfy the relation:

$$\frac{DJ_\Phi}{Dt} = J_\Phi \nabla \cdot \mathbf{s}, \tag{2}$$

with $\frac{DJ_\Phi}{Dt}$ the material derivative of the Jacobian J_Φ and $\mathbf{s}$ the velocity of a point $\mathbf{x} \in \Omega(t)$, which is defined as:

$$\mathbf{s} = \frac{d\mathbf{x}}{dt} = \frac{\partial}{\partial t}\Phi(\tilde{\mathbf{x}}, t). \tag{3}$$

The boundary $\partial\Omega$ of the domain Ω is deforming in time and it is no longer possible to consider the evolution of Ω in a space constructed as the product of a spatial domain $\Omega(t_0)$ and a time interval $[t_0, T]$, with T the final time of the evolution of the flow domain, but we have to consider the space-time domain $\mathcal{E} \subset R^4$ defined as:

$$\mathcal{E} = \cup_{t=t_0}^{T} \Omega(t).$$

The space-time domain $\mathcal{E}$ is bounded by the surfaces $\Omega(t_0)$, $\Omega(T)$ and $\mathcal{Q} = \cup_{t=t_0}^{T} \partial\Omega(t)$. For all $(\mathbf{x}, t) \in \mathcal{E}$ the Euler equations of gas dynamics with respect to an inertial frame can be defined as:

$$\frac{\partial}{\partial t}\mathbf{U}(\mathbf{x}, t) + \frac{\partial}{\partial x_j}\mathbf{F}_j\left(\mathbf{U}(\mathbf{x}, t)\right) = 0, \tag{4}$$

with initial conditions $\mathbf{U}(\mathbf{x}, t_0) = \mathbf{U}_0(\mathbf{x})$, $\mathbf{x} \in \Omega(t_0)$ and boundary conditions $\mathbf{U}(\mathbf{x}, t)|_{\mathcal{Q}} = \mathcal{B}(\mathbf{U}, \mathbf{U}_w, t)$, where $\mathcal{B}$ denotes the boundary operator and $\mathbf{U}_w(t)$ the prescribed boundary flow field data. The summation convention is used on repeated indices in this paper.

The vectors with conserved flow variables $\mathbf{U} : \mathcal{E} \rightarrow R^5$ and fluxes $\mathbf{F}_j$, $j \in \{1, 2, 3\}$; $\mathbf{F}_j : R^5 \rightarrow R^5$, are defined as:

$$\mathbf{U} = \begin{pmatrix} \rho \\ \rho u_i \\ \rho E \end{pmatrix}; \quad \mathbf{F}_j = \begin{pmatrix} \rho u_j \\ \rho u_i u_j + p\delta_{ij} \\ u_j(\rho E + p) \end{pmatrix},$$

where $i \in \{1, 2, 3\}$ and ρ, p, and E denote the density, pressure, and specific total energy, u_i the velocity component in the Cartesian coordinate directions x_i of the velocity vector $\mathbf{u} : \mathcal{E} \rightarrow R^3$,

and δ_{ij} the Kronecker delta symbol. This set of equations is completed with the equation of state for an ideal gas: $p = (\gamma - 1)\rho(E - \frac{1}{2}u_i u_i)$, with γ the ratio of specific heats.

The finite element discretization techniques discussed in the next section belong to the class of Arbitrary Lagrangian Eulerian (ALE) methods. The starting point in the derivations are the Euler equations with respect to an inertial reference frame, Eq. (4), which are transformed into a weak ALE formulation using the mapping Φ, which provides the link between the Eulerian and Lagrangian description of the flow field.

3 Discontinuous Galerkin Discretization for Dynamic Grid Motion

3.1 General Formulation

Consider a partitioning $t_0 < t_1 < \cdots < T$ of the time interval (t_0, T) and denote $I_n = (t_n, t_{n+1})$. Let $\mathcal{T}_h^n$ be a tessellation of a polyhedron domain $\Omega(t)$ at time t_n into a disjunct set of polyhedra K_j^n, $(j \in N^+)$, such that $\overline{\cup K_j^n} = \overline{\Omega}(t_n)$. The space-time domain $\mathcal{E} \subset R^4$ is split into a finite number of space-time elements, which are obtained by splitting the spatial domain $\Omega(t_n)$ into a set of non-overlapping elements $K_j^n \in \mathcal{T}_h^n$ and connecting them with the mapping Φ to the elements $K_j^{n+1} \in \mathcal{T}_h^{n+1}$ at time t_{n+1}. The space-time elements are denoted as $\mathcal{K}_j^{n+1}$. As basic elements in $\Omega(t)$ hexahedra are used, but when topological degeneracies are present, degenerated hexahedra, such as prisms and tetrahedra, are also used. The mapping $\Phi(\check{\mathbf{x}}, t)$ in Eq. (1) is assumed to be sufficiently smooth, orientation preserving and invertible in each interval $t \in I_n$ and is approximated with the mapping $F_{\mathcal{K}}$. Each space-time element is connected to the master element $\hat{\mathcal{K}} = [-1, 1]^4$ by means of the mapping $F_{\mathcal{K}} : (\hat{\mathbf{x}}, \tau) \in \hat{\mathcal{K}} \rightarrow (\mathbf{x}, t) \in \mathcal{K}$, $\hat{\mathbf{x}} = (\xi, \eta, \zeta)^T$, using the standard tri-linear finite element shape functions $\hat{\psi}_i(\hat{\mathbf{x}})$:

$$F_{\mathcal{K}} : (\mathbf{x}, t) = \left(\frac{1}{2} \sum_{i=1}^{m_K} \left(\mathbf{x}_i^n(K) \hat{\psi}_i(\hat{\mathbf{x}})(1 - \tau) + \mathbf{x}_i^{n+1}(K) \hat{\psi}_i(\hat{\mathbf{x}})(1 + \tau) \right), \frac{1}{2}(t_n + t_{n+1}) + \frac{1}{2}(t_{n+1} - t_n)\tau \right), \tag{5}$$

with $\mathbf{x}_i^n(K)$ and $\mathbf{x}_i^{n+1}(K)$ the coordinates of the vertices of element K at times t_n and t_{n+1}, respectively, and m_K the number of vertices in element K, see Fig. 1. The space-time elements $\mathcal{K}_j^{n+1}$ can also be represented as $\mathcal{K}_j^{n+1} = \cup_{t=t_n}^{t_{n+1}} K_j(t)$ with $K_j(t)$ the element K_j at time t. The space-time element $\mathcal{K}_j^{n+1}$ is bounded by K_j^n, K_j^{n+1} and $\partial \mathcal{Q}_j^{n+1} = \cup_{t=t_n}^{t_{n+1}} \partial K_j(t)$.

The discontinuous Galerkin discretization is obtained by approximating the flow field $\mathbf{U}(\mathbf{x}, t)$

and trial functions $\mathbf{W}(\mathbf{x},t)$ with polynomial expansions in each element $\mathcal{K}_j^{n+1}$, which are discontinuous across element faces, both in space and time. The polynomial expansions $\hat{\phi}$ are defined as: $\hat{\phi} = \text{span}\{\hat{\phi}_j, j = 0, \cdots, 4\}$, using the basis functions $\hat{\phi}_j$ which are linear in space and time: $\hat{\phi}_j(\hat{\mathbf{x}},\tau) \in \{1, \xi, \eta, \zeta, \tau\}$.

Define the space $P^1(\mathcal{K}) = \text{span}\{\phi_j = \hat{\phi}_j \circ F_{\mathcal{K}}^{-1}, j = 0, \cdots, 4\}$ then the finite element space $\mathbf{V}_h^1(\mathcal{K})$ is defined as: $\mathbf{V}_h^1(\mathcal{K}) = \{\mathbf{P}(\mathcal{K}) = (p_1, \cdots, p_5)^T | p_i \in P^1(\mathcal{K})\}$. The flow field $\mathbf{U}(\mathbf{x},t)|_{\mathcal{K}}$ can be approximated as:

$$\mathbf{U}_h(\mathbf{x},t) \equiv \mathcal{P}(\mathbf{U}(\mathbf{x},t)|_{\mathcal{K}}) = \sum_{m=0}^{4} \hat{\mathbf{U}}_m(\mathcal{K})\phi_m(\mathbf{x},t), \tag{6}$$

with $\mathcal{P}$ the projection operator to the finite element space $\mathbf{V}_h^1(\mathcal{K})$. The trial functions $\mathbf{W}(\mathbf{x},t)|_{\mathcal{K}}$ are approximated analogously with $\mathbf{W}_h(\mathbf{x},t)$.

The Euler equations (4) in a moving and deforming domain are transformed into a weak formulation: Find $\mathbf{U}_h \in \mathbf{V}_h^1(\mathcal{K})$, such that for all $\mathbf{W}_h \in \mathbf{V}_h^1(\mathcal{K})$:

$$\begin{aligned}
&-\int_{\mathcal{K}_j^{n+1}} \left(\frac{\partial \mathbf{W}_h^T(\mathbf{x},t)}{\partial t} \mathbf{U}_h(\mathbf{x},t) + \frac{\partial \mathbf{W}_h^T(\mathbf{x},t)}{\partial x_k} \mathbf{F}_k(\mathbf{U}_h) \right) d^3x dt + \\
&\int_{\partial \mathcal{Q}_j^{n+1}} \mathbf{W}_h^T(\mathbf{x},t) \left(n_k(\mathbf{x},t)\mathbf{F}_k(\mathbf{U}_h) - \mathbf{n}(\mathbf{x},t) \cdot \mathbf{s}(\mathbf{x},t)\mathbf{U}_h(\mathbf{x},t) \right) dQ + \\
&\int_{K_j^{n+1}} \mathbf{W}_h^T(\mathbf{x},t_{n+1}^-)\mathbf{U}_h(\mathbf{x},t_{n+1}^-) d^3x - \int_{K_j^n} \mathbf{W}_h^T(\mathbf{x},t_n^+)\mathbf{U}_h(\mathbf{x},t_n^-) d^3x = 0,
\end{aligned} \tag{7}$$

with $\mathbf{n}$ the unit normal vector, $\mathbf{s}$ the velocity vector of a point at $\partial\mathcal{Q}_j^{n+1}$, $t_n^{\pm} = \lim_{\epsilon \downarrow 0} t_n \pm \epsilon$ and dQ the Euclidian measure on $\partial\mathcal{Q}_j^{n+1}$. This relation is obtained by multiplying the Euler equations (4) with the trial functions $\mathbf{W}_h$, replacing $\mathbf{U}$ with $\mathbf{U}_h$, and integrating in space and time over the domain $\mathcal{K}_j^{n+1}$. The final form is obtained by partial integration, which has as main benefit that it does not result in loss of conservation under inexact quadrature, Hansbo [8]. The evaluation of the boundary integral in the partial integration process is non-trivial and is most easily done using the general Stokes' theorem. An excellent description of this procedure is given by Bottasso [2]. The last two integrals are obtained by a combination of the time flux after partial integration and the jump condition of the flow field at $t = t_n$:

$$\int_{K_j^n} \mathbf{W}_h^T(\mathbf{x},t_n^+) \left(\mathbf{U}_h(\mathbf{x},t_n^+) - \mathbf{U}_h(\mathbf{x},t_n^-) \right) d^3x = 0,$$

which is added to provide a weak enforcement of the initial condition from the previous time step. This is necessary because the polynomial expansions are discontinuous in time and the expansion in time interval I_n would otherwise not be connected to the previous time interval I_{n-1}.

Introducing the polynomial expansions for $\mathbf{U}_h$ and $\mathbf{W}_h$, Eq. (6), into the weak formulation of the Euler equations the following set of equations for the coefficients $\hat{U}_{mi}(\mathcal{K}_j^{n+1})$ in element $\mathcal{K}_j^{n+1}$ are obtained:

$$-\hat{U}_{mi}(\mathcal{K}_j^{n+1}) \int_{\mathcal{K}_j^{n+1}} \frac{\partial \phi_n(\mathbf{x},t)}{\partial t} \phi_m(\mathbf{x},t) d^3x dt + \hat{U}_{mi}(\mathcal{K}_j^{n+1}) \int_{K_j^{n+1}} \phi_n(\mathbf{x},t_{n+1}^-) \phi_m(\mathbf{x},t_{n+1}^-) d^3x -$$

$$\hat{U}_{mi}(\mathcal{K}_j^{n}) \int_{K_j^{n}} \phi_n(\mathbf{x},t_{n}^+) \phi_m(\mathbf{x},t_{n}^-) d^3x - \int_{\mathcal{K}_j^{n+1}} \frac{\partial \phi_n(\mathbf{x},t)}{\partial x_k} F_{ik}(\mathbf{U}_h) d^3x dt +$$

$$\int_{\partial \mathcal{Q}_j^{n+1}} \phi_n(\mathbf{x},t) n_k(\mathbf{x},t) \left(F_{ik}(\mathbf{U}_h) - s_k(\mathbf{x},t) U_i(\mathbf{x},t) \right) dQ = 0, \qquad i \in \{1, \cdots, 5\},$$

$$n \in \{0, \cdots, 4\}, \quad (8)$$

with F_{ik} the components of the flux vector $\mathbf{F}_k$. The non-linear equations for the expansion coefficients $\hat{\mathbf{U}}(\mathcal{K}_j^{n+1})$, given by Eq. (8), can be expressed as:

$$\left[T(\mathcal{K}_j^{n+1}) \right] \hat{\mathbf{U}}_m(\mathcal{K}_j^{n+1}) = \left[N(\mathcal{K}_j^{n}) \right] \hat{\mathbf{U}}_m(\mathcal{K}_j^{n}) + \triangle t \mathcal{R}_m^{ST}(\mathbf{U}_h), \quad (9)$$

with $\triangle t = t_{n+1} - t_n$. The matrix $[T]$ contains the contribution of the first and second integral in Eq. (8) and the elements of matrix $[N]$ consist of the third integral in Eq. (8). The components of the residual vector $\mathcal{R}_m^{ST}$ are given by the last two integrals in Eq. (8), divided by $\triangle t$. The solution of this set of non-linear equations is discussed in Section 6. The second and third integral in Eq. (8) are closely related to the mass matrix of the space discontinuous Galerkin discretization of the element at time levels $t = t_n$ and $t = t_{n+1}$ if the grid motion is continuous between different time levels, which is assumed to be the case in this paper. Analytic expressions for these integrals are given in Van der Vegt and Van der Ven [25]. The first integral in Eq. (8) can be further evaluated as:

$$\begin{aligned}
\int_{\mathcal{K}} \frac{\partial \phi_n(\mathbf{x},t)}{\partial t} \phi_m(\mathbf{x},t) d^3x dt &= 0, && n = 0, \\
&= \int_{\hat{\mathcal{K}}} J_n(\hat{\mathbf{x}},\tau) \hat{\phi}_m(\hat{\mathbf{x}},\tau) d^3\hat{x} d\tau, && n = 1,2,3, \\
&= \int_{\hat{\mathcal{K}}} J_0(\hat{\mathbf{x}},\tau) \hat{\phi}_m(\hat{\mathbf{x}},\tau) d^3\hat{x} d\tau, && n = 4, \quad (10)
\end{aligned}$$

with the Jacobian matrices J_k defined as:

$$J_0(\hat{\mathbf{x}},\tau) = \det(\mathbf{x}_\xi, \mathbf{x}_\eta, \mathbf{x}_\zeta) \quad (11)$$

$$J_1(\hat{\mathbf{x}},\tau) = -\det(\mathbf{x}_\eta, \mathbf{x}_\zeta, \mathbf{x}_\tau) \quad (12)$$

$$J_2(\hat{\mathbf{x}},\tau) = \det(\mathbf{x}_\zeta, \mathbf{x}_\tau, \mathbf{x}_\xi) \quad (13)$$

$$J_3(\hat{\mathbf{x}},\tau) = -\det(\mathbf{x}_\tau, \mathbf{x}_\xi, \mathbf{x}_\eta). \quad (14)$$

Here $\mathbf{x}_\xi$, $\mathbf{x}_\eta$, $\mathbf{x}_\zeta$, and $\mathbf{x}_\tau$ denote derivatives of $\mathbf{x}$ with respect to the local coordinates ξ, η, ζ, and τ of the master element $\hat{\mathcal{K}}$. These relations are obtained using the transformation $F_\mathcal{K}$ from $\hat{\mathcal{K}}$ to $\mathcal{K}$, Eq. (5), and the relation $\phi_n = \hat{\phi}_n \circ F_\mathcal{K}^{-1}$. The integrals in Eq. (10) are calculated numerically using Gauss quadrature rules of sufficient degree to be exact. They can be calculated analytically, but this does not result in significantly less computational work, as contrasted with the element face and volume flux integrals where the analytical results are considerably simpler.

3.2 Discontinuous Galerkin Formulation using Moving Reference Systems

Many applications, e.g. oscillating wings and propellers, can be well described if the computational flow domain is moving (translating-rotating) with the same motion as the moving object. The domain motion can be described using the coordinate transformation:

$$\mathbf{x}^{(0)}(t) = \mathcal{C}(t)\mathbf{x}^{(1)} + \mathbf{r}^{(0)}(t), \tag{15}$$

with $\mathcal{C}(t)$ the rotation matrix between the inertial and moving reference frame and $\mathbf{r}^{(0)}(t)$ the position of the origin of the moving reference system. The superscripts $^{(0)}$ and $^{(1)}$ indicate if a vector has components relative to the inertial or moving reference system. If there is no danger of ambiguity the superscript $^{(0)}$ is omitted in the remainder of this paper. The Jacobian of the transformation between the two coordinate systems, given by Eq. (15), is defined as:

$$J = \det \left| \frac{\partial \mathbf{x}^{(0)}}{\partial \mathbf{x}^{(1)}} \right| = \det(\mathcal{C}(t)),$$

and $J = 1$ for rigid body translation and rotation. The domain $\Omega(t)$ becomes independent of time when expressed relative to the moving reference frame $O_1X_1Y_1Z_1$ and is denoted $\Omega^{(1)}$. The domain $\Omega^{(1)}$ is split into a disjunct set of hexahedral elements $K_j^{(1)} \in \mathcal{T}_h$, with $\overline{\cup K_j^{(1)}} = \overline{\Omega^{(1)}}$.

The derivation of the weak formulation of the Euler equations in a moving reference frame is most easily started from the general semi-discrete weak formulation for a moving element $K_j(t)$:

$$\begin{aligned} &\frac{d}{dt}\int_{K_j(t)} \mathbf{W}_h^T(\mathbf{x})\mathbf{U}_h(\mathbf{x},t)d^3x + \\ &\int_{K_j(t)} \mathbf{W}_h^T(\mathbf{x})\frac{\partial}{\partial x_k}\left(\mathbf{F}_k(\mathbf{U}_h) - s_k(\mathbf{x},t)\mathbf{U}_h(\mathbf{x},t)\right)d^3x = 0. \end{aligned} \tag{16}$$

This relation is obtained by multiplying the Euler equations, Eq. (4), with the trial functions $\mathbf{W}_h$, integrating over the domain occupied by element $K_j(t)$ and using the relation for the Jacobian J_Φ of the mapping between the element $K_j(t)$ and $K_j^{(1)}$ in the moving reference system, Eq. (2).

It is important to note that the components of vector valued quantities in Eq. (16) are still expressed relative to the inertial reference system, otherwise source terms related to the Coriolis force would appear in the formulation. The weak formulation of the Euler equations is further refined using the transformation from the inertial to the moving reference frame, Eq. (15), and partial integration:

$$\frac{d}{dt}\int_{K_j^{(1)}} \mathbf{W}_h^{*T}(\mathbf{x}^{(1)})\mathbf{U}_h^*(\mathbf{x}^{(1)},t)d^3x^{(1)} +$$

$$\int_{\partial K_j^{(1)}} \mathbf{W}_h^{*T}(\mathbf{x}^{(1)})\left(n_k(\mathbf{x}^{(1)},t)\mathbf{F}_k(\mathbf{U}_h^*) - \mathbf{n}^{(1)}(\mathbf{x}^{(1)})\cdot\mathbf{s}^{(1)}(\mathbf{x}^{(1)},t)\mathbf{U}_h^*(\mathbf{x}^{(1)},t)\right)dS^{(1)} -$$

$$\int_{K_j^{(1)}} \frac{\partial \mathbf{W}_h^{*T}(\mathbf{x}^{(1)})}{\partial x_k^{(1)}}\left(\mathbf{F}_p(\mathbf{U}_h^*)\mathcal{C}_{pk}(t) - s_k^{(1)}(\mathbf{x}^{(1)},t)\mathbf{U}_h^*(\mathbf{x}^{(1)},t)\right)d^3x^{(1)} = 0, \tag{17}$$

with $\mathbf{W}_h^*(\mathbf{x}^{(1)}) = \mathbf{W}_h(\mathbf{x}^{(0)})$ and $\mathbf{U}_h^*(\mathbf{x}^{(1)},t) = \mathbf{U}_h(\mathbf{x}^{(0)},t)$. In the derivation of Eq. (17) the relations $n_k^{(1)} = C_{jk}n_j$ and $s_k^{(1)} = C_{jk}s_j$ are used, with the matrix $\mathcal{C}_{pk}(t)$ defined as:

$$\mathcal{C}_{pk}(t) = \frac{\partial x_k^{(1)}}{\partial x_p}.$$

For efficiency reasons a mixed formulation is used with vectors having components both in the inertial and moving reference frame, because in this case the conservation form will be maintained and no source terms appear. The formulation given by Eq. (17) has as main benefit that the geometric contributions do not depend on time. This makes it possible to pre-calculate these contributions, resulting in a significant savings in computing time compared to the general formulation discussed in the previous section.

The polynomial expansions for $\mathbf{U}_h^*$ and $\mathbf{W}_h^*$ are defined using the mapping $F_K^{(1)} : \hat{\mathbf{x}} \in \hat{K}^{(1)} \rightarrow \mathbf{x}^{(1)} \in K^{(1)}$:

$$F_K^{(1)} : \mathbf{x}^{(1)} = \sum_{i=1}^{m_K} \mathbf{x}_i^{(1)}(K^{(1)})\hat{\psi}_i(\hat{\mathbf{x}}), \tag{18}$$

with $\mathbf{x}_i^{(1)}(K^{(1)})$ the vertices of the hexahedral element $K^{(1)}$ with $m_K = 8$, $\hat{K}^{(1)} = [-1,1]^3$ and $\hat{\psi}_i(\hat{\mathbf{x}})$ the tri-linear finite element shape functions. The flow field $\mathbf{U}_h^*$ in each element in the moving reference frame is approximated as:

$$\mathbf{U}_h^* = \sum_{m=0}^{3} \hat{\mathbf{U}}_m(K_j^{(1)},t)\phi_m^*(\mathbf{x}^{(1)}),$$

with an equivalent expression for the trial function $\mathbf{W}_h^*$, which, however, does not depend on time. The basis functions $\phi_m^*(\mathbf{x}^{(1)})$ are defined completely analogously as for the space-time elements

discussed in Section 3.1, except that they only depend on the spatial coordinate $\mathbf{x}^{(1)}$. For more details see Van der Vegt and Van der Ven [25]. Introducing the polynomial expansions for $\mathbf{U}_h^*$ and $\mathbf{W}_h^*$ into the weak formulation for the Euler equations in a moving reference frame results in the following set of equations for the coefficients $\hat{\mathbf{U}}_m(K_j,t)$:

$$\frac{d}{dt}\hat{U}_{mi}(K_j,t)\int_{K_j^{(1)}}\phi_n^*(\mathbf{x}^{(1)})\phi_m^*(\mathbf{x}^{(1)})d^3x^{(1)}+$$

$$\int_{\partial K_j^{(1)}}\phi_n^*(\mathbf{x}^{(1)})\left(n_k(\mathbf{x}^{(1)},t)F_{ik}(\mathbf{U}_h^*)-n_k^{(1)}(\mathbf{x}^{(1)})s_k^{(1)}(\mathbf{x}^{(1)},t)U_i^*(\mathbf{x}^{(1)},t)\right)dS^{(1)}-$$

$$\int_{K_j^{(1)}}\frac{\partial\phi_n^*(\mathbf{x}^{(1)})}{\partial x_k^{(1)}}\left(F_{ip}(\mathbf{U}_h^*)\mathcal{C}_{pk}(t)-s_k^{(1)}(\mathbf{x}^{(1)},t)U_i^*(\mathbf{x}^{(1)},t)\right)d^3x^{(1)}=0,\qquad i\in\{1,\cdots,5\},$$

$$n\in\{0,\cdots,3\}. \quad (19)$$

The first integral in Eq. (19) is the mass matrix of the moving elements and needs to be calculated only once since the grid is not deforming. An analytic expression for this integral can be found in [25]. For use in the time integration method it is beneficial to express Eq. (19) symbolically as:

$$[M]\,\frac{d}{dt}\hat{\mathbf{U}}_m=\mathcal{R}_m^{MR}(\mathbf{U}_h), \quad (20)$$

with the elements of the mass matrix $[M]$ given by the first integral in Eq. (19) and the residual vector $\mathcal{R}_m^{MR}$ by the last two integrals in Eq. (19).

4 Flux Calculation

The polynomial expansions for the flow field $\mathbf{U}_h$ and trial functions $\mathbf{W}_h$ are discontinuous at element faces. The flux at element faces therefore is multi-valued and requires special treatment. The discontinuity in space can be interpreted as a Riemann problem and the (approximate) solution of the Riemann problem can be used to define the flux at element faces. This is accomplished by replacing the flux function with a monotone Lipschitz flux $\mathbf{H}(\mathbf{U}_L,\mathbf{U}_R)$, which is consistent, $\mathbf{H}(\mathbf{U},\mathbf{U})=\hat{\mathbf{F}}(\mathbf{U})\equiv n_j\mathbf{F}_j(\mathbf{U})$. Here $\mathbf{U}_L$ and $\mathbf{U}_R$ denote the left and right state in the Riemann problem. Any of the well-known (approximate) Riemann solvers, such as those from Godunov, Roe, Lax-Friedrichs, or Osher, can be used to accomplish this. A significant benefit of this approach is that upwinding is introduced into the finite element formulation and a scheme with excellent shock capturing capability is obtained. See for instance the calculations of the lambda shock wave on the ONERA M6 wing using a discontinuous Galerkin discretization in [25].

In this paper the Osher scheme is used. A detailed description of the calculation of the Osher flux in multiple dimensions, including boundary conditions, can be found in Osher and Chakravarthy [17]. In case of dynamic grid motion some small modifications to the Osher scheme must be made. The approximate Riemann solver must be based on the complete flux, including the grid motion contribution, because the flow field $\mathbf{U}_h$ at element faces is also multi-valued. The monotone Lipschitz flux $\mathbf{H}^c(\mathbf{U}_h^{\mathrm{int}(K)}, \mathbf{U}_h^{\mathrm{ext}(K)})$ which satisfies:

$$\mathbf{H}^c(\mathbf{U}_h^{\mathrm{int}(K)}, \mathbf{U}_h^{\mathrm{ext}(K)}) = \hat{\mathbf{F}}^c(\mathbf{U}_h) \equiv n_k \mathbf{F}_k(\mathbf{U}_h) - \mathbf{n} \cdot \mathbf{s}\, \mathbf{U}_h,$$

is approximated with the Osher flux difference formulation. Here $\mathrm{int}(K)$ and $\mathrm{ext}(K)$ denote the value of $\mathbf{U}_h$ at $\mathbf{x} \in \partial K$ taken as the limit from the interior and exterior of K.

The main reasons for using the Osher flux difference scheme is that it is a very accurate method with good shock capturing capabilities, which does not require an entropy fix, and is well suited for both inviscid and viscous flows [22], because it has a low numerical dissipation. Boundary conditions can be introduced in the Osher scheme by solving the Riemann initial-boundary value problem and a uniform flux formulation is obtained, both at interior and exterior element faces, which fits very well into the discontinuous Galerkin discretization. The Osher approximate Riemann solver for problems without grid motion is described in [17]. In case of dynamic grid motion the Osher scheme is defined as:

$$\mathbf{H}^c(\mathbf{U}_h^{\mathrm{int}(K)}, \mathbf{U}_h^{\mathrm{ext}(K)}) = \tfrac{1}{2}\left(\hat{\mathbf{F}}^c(\mathbf{U}_h^{\mathrm{int}(K)}) + \hat{\mathbf{F}}^c(\mathbf{U}_h^{\mathrm{ext}(K)}) - \sum_\alpha \int_{\Gamma_\alpha(\mathbf{U}_h^{\mathrm{int}(K)}, \mathbf{U}_h^{\mathrm{ext}(K)})} |\partial \hat{\mathbf{F}}^c| d\Gamma \right),$$

where $\cup_\alpha \Gamma_\alpha$ is a path in phase space between $\mathbf{U}_h^{\mathrm{int}(K)}$ and $\mathbf{U}_h^{\mathrm{ext}(K)}$ and $\partial \hat{\mathbf{F}}^c$ the Jacobian of the flux vector $\hat{\mathbf{F}}^c$. The main difference in calculating the Osher flux for moving elements in comparison with non-moving elements is that the eigenvalues λ used in determining the different parts of the path integrals Γ_α must be corrected for the grid velocity: $\lambda_{1,2,3} = \mathbf{n} \cdot (\mathbf{u} - \mathbf{s})$ and $\lambda_{4,5} = \mathbf{n} \cdot (\mathbf{u} - \mathbf{s}) \pm c$, with $\mathbf{u}$ and $\mathbf{s}$ the fluid and grid velocity vectors, respectively, and c the speed of sound. The relations for the intermediate states $\mathbf{U}^\alpha$ in the Osher flux do not change, except for the condition at a sonic point. The Osher flux for moving element faces can be split into the standard Osher flux for non-moving grids and a part directly related to the grid velocity:

$$\mathbf{H}^c(\mathbf{U}_h^{\mathrm{int}(\mathcal{K})}, \mathbf{U}_h^{\mathrm{ext}(\mathcal{K})}) = \mathbf{H}(\mathbf{U}_h^{\mathrm{int}(\mathcal{K})}, \mathbf{U}_h^{\mathrm{ext}(\mathcal{K})}) - \mathbf{n} \cdot \mathbf{s}\, \mathbf{G}(\mathbf{U}_h^{\mathrm{int}(\mathcal{K})}, \mathbf{U}_h^{\mathrm{ext}(\mathcal{K})}), \tag{21}$$

where the flux vector $\mathbf{G}$ is obtained by replacing the normal flux vector $n_k \mathbf{F}_k(\mathbf{U})$ in the Osher flux with $\mathbf{U}_h$. The calculation of the flux vector $\mathbf{G}$ does not require additional calculations, because

all information is already available after calculating the Osher flux contribution which does not depend on grid motion. As an alternative to the Osher scheme the Roe flux difference scheme for moving element faces, as described by Harten and Hyman [10], could also be used, but this method requires an entropy fix to prevent expansion shocks.

The flux integration over the element faces and volumes, both in space and time, requires special care. Cockburn et al. [5] derived conditions for the flux integration based on Gauss quadrature rules when there is no dynamic grid motion. These conditions are not sufficient for a second-order accurate scheme which also must satisfy the Geometric Conservation Law (GCL). The GCL requires that a uniform flow field is not disturbed by the grid motion and is originally formulated by Thomas and Lombard [21]. The GCL is a non-trivial condition and is most easily satisfied if the geometric contributions are calculated exactly. This would require for instance a nine-point product Gauss quadrature rule for the spatial integration of the element faces and a twenty-seven point Gauss quadrature rule for the volume flux integrals in case of the DG discretization in a translating-rotating reference frame. This would result in a prohibitively expensive discretization because of the large number of flux calculations. It is possible to use more sophisticated quadrature rules, as described by Stroud [20], but this does not sufficiently improve efficiency.

The use of Gauss quadrature rules can be circumvented using special face and element flux averages and analytically or numerically calculated exact geometric contributions. This method results in a second-order accurate discretization and was proposed and analyzed in detail by Van der Vegt and Van der Ven [25] and is also used in this paper for the space-time flux integrals and the flux integrals for the discretization in a moving reference frame. The main benefit of this method is that only one flux calculation for each element face is necessary and relatively simple and exact relations for the geometric contributions are obtained, which therefore automatically satisfy the GCL.

4.1 Approximation of Flux Integrals for the Space-Time Formulation

The boundary surfaces $\partial\mathcal{Q}_j^{n+1}$ of the space-time elements are split into a finite number of non-overlapping faces $\mathcal{S}_\mathcal{K}^p = \cup_{t=t_n}^{t_{n+1}} e_K^p(t)$, $p \in \{1, \cdots, 6\}$, with e_K^p one of the six faces of the hexahedron $K(t)$ which constitutes the space-time element $\mathcal{K}$, see Fig. 1. The space-time flux integrals in Eq.

(8) then can be approximated as:

$$\begin{aligned}\int_{\mathcal{S}_{\mathcal{K}}^p} \phi_n(\mathbf{x},t) H_i^c(\mathbf{U}_h^{\mathrm{int}(\mathcal{K})}, \mathbf{U}_h^{\mathrm{ext}(\mathcal{K})}) dQ \;\cong\; & \tfrac{1}{2}\left(F_{ik}(\bar{\mathbf{U}}_h^{\mathrm{int}(\mathcal{K})}) + F_{ik}(\bar{\mathbf{U}}_h^{\mathrm{ext}(\mathcal{K})})\right) \int_{\mathcal{S}_{\mathcal{K}}^p} \phi_n(\mathbf{x},t) n_k(\mathbf{x},t) dQ - \\ & \tfrac{1}{2}\left(\sum_\alpha \int_{\Gamma_\alpha(\bar{\mathbf{U}}_h^{\mathrm{int}(\mathcal{K})}, \bar{\mathbf{U}}_h^{\mathrm{ext}(\mathcal{K})})} |\partial\hat{\mathbf{F}}| d\Gamma\right) \int_{\mathcal{S}_{\mathcal{K}}^p} \phi_n(\mathbf{x},t) dQ - \\ & G_i(\bar{\mathbf{U}}_h^{\mathrm{int}(\mathcal{K})}, \bar{\mathbf{U}}_h^{\mathrm{ext}(\mathcal{K})}) \int_{\mathcal{S}_{\mathcal{K}}^p} \phi_n(\mathbf{x},t) n_k(\mathbf{x},t) s_k(\mathbf{x},t) dQ, \\ & \qquad\qquad i \in \{1, \cdots, 5\}, \\ & \qquad\qquad n \in \{0, \cdots, 4\}, \quad (22)\end{aligned}$$

with H_i, F_{ik} and G_i the elements of the vectors $\mathbf{H}$, $\mathbf{F}_k$ and $\mathbf{G}$. Analytic expressions for the integrals $\int_{\mathcal{S}_{\mathcal{K}}^p} \phi_n \mathbf{n} dQ$ and $\int_{\mathcal{S}_{\mathcal{K}}^p} \phi_n \mathbf{n} \cdot \mathbf{s} dQ$ are given in the Appendix A.1, whereas the integrals $\int_{\mathcal{S}_{\mathcal{K}}^p} \phi_n dQ$ are calculated numerically. The use of analytic relations is beneficial because they generally require significantly less work than the use of Gauss quadrature rules and they must be calculated each time when the grid is changing. The integrals $\int_{\mathcal{S}_{\mathcal{K}}^p} \phi_n dQ$ do not need to be calculated exactly in order to satisfy the GCL, because the contribution of the Osher flux integral is zero in case of uniform flow. The flow states $\bar{\mathbf{U}}_h = \frac{1}{|\mathcal{S}_{\mathcal{K}}^p|} \int_{\mathcal{S}_{\mathcal{K}}^p} \mathbf{U}_h(\mathbf{x},t) dQ$ in the element faces, with $|\mathcal{S}_{\mathcal{K}}^p|$ the area of the space-time face $\mathcal{S}_{\mathcal{K}}^p$, are defined as:

$$\bar{\mathbf{U}}_h^{\mathrm{int}(\mathcal{K})} = \frac{1}{|\mathcal{S}_{\mathcal{K}}^p|} \sum_{m=0}^{4} \hat{\mathbf{U}}_m(\mathcal{K}) \int_{\mathcal{S}_{\mathcal{K}}^p} \phi_{m,\mathcal{K}}(\mathbf{x},t) dQ, \quad (23)$$

$$\bar{\mathbf{U}}_h^{\mathrm{ext}(\mathcal{K})} = \frac{1}{|\mathcal{S}_{\mathcal{K}}^p|} \sum_{m=0}^{4} \hat{\mathbf{U}}_m(\mathcal{K}') \int_{\mathcal{S}_{\mathcal{K}}^p} \phi_{m,\mathcal{K}'}(\mathbf{x},t) dQ, \quad (24)$$

with $\mathcal{K}'$ the index of the element connected to element $\mathcal{K}$ at the face $\mathcal{S}_{\mathcal{K}}^p$. The suffices $\mathcal{K}$ and $\mathcal{K}'$ of $\phi_m(\mathbf{x},t)$ refer to the limit of $\phi_m(\mathbf{x},t)$ taken from the interior and exterior of element $\mathcal{K}$ at the face $\mathcal{S}_{\mathcal{K}}^p$, respectively. The volume flux integrals in Eq. (8) can be approximated as:

$$\begin{aligned}\int_{\mathcal{K}} \frac{\partial \phi_n(\mathbf{x},t)}{\partial x_k} F_{ik}(\mathbf{U}_h) d^3x dt \;=\; & 0, && \text{if} \quad n = 0, 4, \\ \cong\; & \tfrac{1}{2}(t_{n+1} - t_n) F_{ik}(\bar{\mathbf{U}}_h) \int_{\hat{\mathcal{K}}} S_k^n(\hat{\mathbf{x}},\tau) d^3\hat{x} d\tau, && \text{if} \quad n = 1, 2, 3, \end{aligned} \quad (25)$$

with S_k^n the elements of the metrical coefficients $\mathbf{S}^n(\hat{\mathbf{x}},\tau)$ defined as:

$$\begin{aligned}\mathbf{S}^1(\hat{\mathbf{x}},\tau) &= \mathbf{x}_\eta \times \mathbf{x}_\zeta \\ \mathbf{S}^2(\hat{\mathbf{x}},\tau) &= \mathbf{x}_\zeta \times \mathbf{x}_\xi \\ \mathbf{S}^3(\hat{\mathbf{x}},\tau) &= \mathbf{x}_\xi \times \mathbf{x}_\eta.\end{aligned}$$

The analytic calculation of the geometric contributions on the right hand side of Eq. (25) is discussed in Appendix A.1. The mean flow field $\bar{\mathbf{U}}_h$ for the volume integrals is defined as:

$$\bar{\mathbf{U}}_h = \frac{1}{|\mathcal{K}|}\sum_{m=0}^{4}\hat{\mathbf{U}}_m \int_{\mathcal{K}} \phi_m(\mathbf{x},t)d^3xdt = \frac{(t_{n+1}-t_n)}{2|\mathcal{K}|}\sum_{m=0}^{4}\hat{\mathbf{U}}_m \int_{\hat{\mathcal{K}}} \hat{\phi}_m(\hat{\mathbf{x}},\tau)J_0(\hat{\mathbf{x}},\tau)d^3\hat{x}d\tau, \tag{26}$$

with $|\mathcal{K}|$ the volume of the space-time element $\mathcal{K}$ and the Jacobian J_0 given by Eq. (11). The space-time formulation automatically satisfies the GCL, because the geometric contributions, which are the only relevant components for satisfying the GCL because the flow field is assumed uniform, are calculated exactly, either analytically or numerically with Gauss quadrature rules.

4.2 Approximation of Flux Integrals for Moving Reference Systems

The splitting of the Osher flux in a part which does not depend on the grid motion and a part directly related to the grid velocity, Eq. (21), is also used for calculating the flux integrals in a moving reference system. The calculation of the flux contribution not related to the grid motion is discussed in detail in Van der Vegt and Van der Ven [25] and follows the same approach as used for the space-time formulation, but with the integration restricted to the spatial part. The flux contribution at element faces which is related to the body motion is evaluated using the representation for the velocity of the moving reference frame:

$$\frac{d\mathbf{x}^{(0)}}{dt} = \mathbf{s}^{(0)}(t) = \mathbf{v}^{(0)}(t) + \omega^{(1)}(t)\times\mathbf{r}_b^{(1)}, \tag{27}$$

with $\mathbf{v}^{(0)}$ the velocity vector of the origin of the moving reference frame, $\omega^{(1)}$ the angular velocity vector of the moving reference frame and $\mathbf{r}_b^{(1)} = \mathbf{x}^{(1)} - \mathbf{x}_b^{(1)}$ the vector pointing from the center of rotation $\mathbf{x}_b^{(1)}$ in coordinate system $O_1X_1Y_1Z_1$ to a point $\mathbf{x}^{(1)}$ in this reference system. Introducing the representation for the grid velocity $\mathbf{s}$ the approximation to the element face flux integrals is obtained:

$$\begin{aligned}\int_{\partial K_j^{(1)}} \phi_n^*(\mathbf{x}^{(1)})n_k^{(1)}(\mathbf{x}^{(1)})s_k^{(1)}(\mathbf{x}^{(1)},t)G_i dS^{(1)} \;\cong\; & \bar{G}_i(t)\left(v_{0k}^{(1)}(t)\int_{\partial K_j^{(1)}}\phi_n^*(\mathbf{x}^{(1)})n_k^{(1)}(\mathbf{x}^{(1)})dS^{(1)} + \right.\\ & \left.\omega_k^{(1)}(t)\int_{\partial K_j^{(1)}}(\mathbf{r}_b^{(1)}\times\mathbf{n}^{(1)})_k\phi_n^*(\mathbf{x}^{(1)})dS^{(1)}\right).\end{aligned} \tag{28}$$

with $\bar{G}_i(t) = G_i(\bar{\mathbf{U}}_h^{\mathrm{int}(K^{(1)})}(t), \bar{\mathbf{U}}_h^{\mathrm{ext}(K^{(1)})}(t))$. The volume flux integrals are calculated analogously:

$$\int_{K_j^{(1)}} \frac{\partial \phi_n^*(\mathbf{x}^{(1)})}{\partial x_k^{(1)}} s_k^{(1)}(\mathbf{x}^{(1)}, t) U_i(\mathbf{x}^{(1)}, t) d^3x^{(1)} \quad \cong \quad \bar{U}_i(t) \left(v_{0k}^{(1)}(t) \int_{K_j^{(1)}} \frac{\partial \phi_n^*(\mathbf{x}^{(1)})}{\partial x_k^{(1)}} d^3x^{(1)} + \right.$$
$$\left. \omega_k^{(1)}(t) \int_{K_j^{(1)}} \left(\mathbf{r}_b^{(1)} \times \frac{\partial \phi_n^*(\mathbf{x}^{(1)})}{\partial \mathbf{x}^{(1)}} \right)_k d^3x^{(1)} \right). \quad (29)$$

The integrals on the right hand side of Eqs. (28) and (29) are calculated analytically and are discussed in the Appendix A.2. The use of these analytical relations guarantees that the Geometric Conservation Law (GCL) is satisfied if the contribution of the steady fluxes satisfies the Surface Conservation Law (SCL):

$$\int_{\partial K_j^{(1)}} \phi_n^*(\mathbf{x}^{(1)}) n_k(\mathbf{x}^{(1)}, t) F_{ik}(\mathbf{U}_h) dS^{(1)} - \int_{K_j^{(1)}} \frac{\partial \phi_n^*(\mathbf{x}^{(1)})}{\partial x_k^{(1)}} \mathcal{C}_{pk}(t) F_{ip}(\mathbf{U}_h) d^3x^{(1)} = 0,$$

for a uniform flow field $\mathbf{U}$. This condition is automatically satisfied with the flux approximation for the steady part using the discretization technique discussed in Van der Vegt and Van der Ven [25] and results in a second-order accurate spatial discretization.

5 Slope Limiter

The discontinuous Galerkin finite element method requires a slope limiting algorithm to obtain monotone solutions. Cockburn et al. [5] derived a local projection limiter which guarantees monotonicity for multi-dimensional scalar equations, but this method is not straightforward to use. In this paper the slope limiter derived by Barth and Jespersen [1], with the modifications proposed by Venkatakrishnan [28], is used. The application of this limiter to the DG method and the corrections necessary to maintain a conservative scheme are discussed in detail in Van der Vegt and Van der Ven [25]. This limiter is effective in capturing shocks in transonic flows without numerical oscillations.

The limiting procedure for the DG discretization in a translating-rotating reference frame can be summarized as follows. The limiter uses the element average $\bar{\mathbf{U}}_K = \frac{1}{|K|} \int_K \mathbf{U}_h(\mathbf{x}) d\Omega$, with $|K|$ the volume of element K, and the local minimum and maximum of the flow field defined for each component $\bar{U}_{i,K}$, $i = \{1, \cdots, 5\}$ as:

$$\begin{aligned} U_{i,K}^{\min} &= \min_{\forall K' \in N(K)} (\bar{U}_{i,K}, \bar{U}_{i,K'}), \\ U_{i,K}^{\max} &= \max_{\forall K' \in N(K)} (\bar{U}_{i,K}, \bar{U}_{i,K'}), \end{aligned}$$

with $N(K)$ the set of neighboring elements which connect to element K at the faces S_K^p and $\bar{U}_{i,K'}$ the neighboring element averages. The limiter function Ψ is defined as:

$$\Psi_{i,K} = \min_{\forall s_K^p \neq \emptyset} \begin{cases} \frac{\triangle_+^2 + \epsilon_{m,K}^2 + 2\triangle\triangle_+}{\triangle_+^2 + \epsilon_{m,K}^2 + 2\triangle^2 + \triangle\triangle_+}, & \text{if} \quad \triangle > 0, \\ \frac{\triangle_-^2 + \epsilon_{m,K}^2 + 2\triangle\triangle_-}{\triangle_-^2 + \epsilon_{m,K}^2 + 2\triangle^2 + \triangle\triangle_-}, & \text{if} \quad \triangle < 0, \\ 1, & \text{if} \quad \triangle = 0, \end{cases}$$

with $\triangle = U_{i,K}^* - \bar{U}_{i,K}$, $\triangle_+ = U_{i,K}^{\max} - \bar{U}_K$ and $\triangle_- = U_{i,K}^{\min} - \bar{U}_K$. Here $U_{i,K}^*$ denotes the value of $U_{i,K}$ at the location where the flux must be calculated. The coefficients $\epsilon_{m,K}$ are set equal to $\epsilon_{m,K} = (C\triangle_{m,K})^3$, with $\triangle_{m,K}$ the minimum distance between the element face centers of two opposite faces of element K in the local directions ξ, η or ζ of the master element $\hat{K}$. The limiting operation can now be expressed as:

$$\tilde{U}_{mi} = \Pi_{mni}(\mathbf{U}_h)\hat{U}_{ni}, \qquad i \in \{1, \cdots, 5\},\ m \in \{0, \cdots, 3\},$$

no summation on i,

with

$$\Pi_{mni}(\mathbf{U}_h) = \begin{pmatrix} 1 & (1-\Psi_i)M_{1,0}/M_{0,0} & (1-\Psi_i)M_{2,0}/M_{0,0} & (1-\Psi_i)M_{3,0}/M_{0,0} \\ 0 & \Psi_i & 0 & 0 \\ 0 & 0 & \Psi_i & 0 \\ 0 & 0 & 0 & \Psi_i \end{pmatrix}. \tag{30}$$

In case of the space-time DG discretization the same limiting procedure is used, but with the element averages based on $\mathcal{K}$ and the faces S_K^p replaced by $\mathcal{S}_\mathcal{K}^p$. No limiting is done on the components $\hat{U}_{4,i}$ of the expansion in time.

6 Implicit Time Integration

Calculations of unsteady flows frequently suffer from a large disparity between the physically relevant time scales and the time step limitations imposed by the stability constraints of explicit time integration methods. These limitations can be alleviated for the discontinuous Galerkin methods presented in this paper by using the implicit time integration methods discussed in this section. Special attention will be paid to the solution of the non-linear equations for the flow field expansion coefficients obtained with these implicit formulations. The Space-Time Discontinuous Galerkin (STDG) finite element method, discussed in Section 3.1, results already in an implicit formulation,

both in space and time. An implicit formulation for the DG discretization using a moving reference frame, further denoted as MRDG, is obtained with an implicit approximation to the $\partial\tilde{\mathbf{U}}_m/\partial t$ contribution in the semi-discrete formulation given by Eq. (20). The resulting set of non-linear equations for both methods are solved by augmenting the equations with a weighted pseudo-time derivative of the flow field expansion coefficients and marching the solution in pseudo-time to a steady state using the Full Approximation Storage (FAS) multigrid algorithm. The use of the FAS algorithm to solve the equations of an implicit time discretization of the Euler and Navier-Stokes equations was first proposed by Jameson [11], and made unconditionally stable by Melson et al. [14]. The non-linear equations for the DG discretizations, which can be represented as $\mathcal{L}_m(\tilde{\mathbf{U}}_m^{n+1}, \tilde{\mathbf{U}}_m^n, \tilde{\mathbf{U}}_m^{n-1}) = 0$, are now solved by integrating the system of equations in pseudo-time till a sufficiently accurate steady state solution $\tilde{\mathbf{U}}_m$ is obtained:

$$[M]\,\frac{\partial\tilde{\mathbf{U}}_m}{\partial\tau} = \mathcal{L}_m(\tilde{\mathbf{U}}_m, \tilde{\mathbf{U}}_m^n, \tilde{\mathbf{U}}_m^{n-1}), \tag{31}$$

which then is equal to $\tilde{\mathbf{U}}_m^{n+1}$. Here the mass matrix $[M]$ for the STDG method is defined as:

$$M_{nm} = \int_{\mathcal{K}_j^{n+1}} \phi_n(\mathbf{x},t)\phi_m(\mathbf{x},t)d^3xdt, \qquad\qquad n,m \in \{0,\cdots,4\},$$

and $\tilde{\mathbf{U}}_m$ refers to the limited expansion coefficients, which are obtained with the limiting procedure discussed in the previous section. The mass matrix $[M]$ for the MRDG finite element method is identical to the one in Eq. (20). The operator $\mathcal{L}_m$ for the STDG finite element method is defined as:

$$\mathcal{L}_m^{ST}(\tilde{\mathbf{U}}_m, \tilde{\mathbf{U}}_m^n) = \mathcal{R}_m^{ST}(\tilde{\mathbf{U}}_h) + \left(\left[N(\mathcal{K}_j^n)\right]\tilde{\mathbf{U}}_m(\mathcal{K}_j^n) - \left[T(\mathcal{K}_j^{n+1})\right]\tilde{\mathbf{U}}_m(\mathcal{K}_j^{n+1})\right)/\triangle t,$$

with $\mathcal{R}^{ST}$, $[N]$ and $[T]$ defined in Eq. (9) and $\tilde{\mathbf{U}}_m^n = \tilde{\mathbf{U}}_m(\mathcal{K}_j^n)$. The operator $\mathcal{L}_m$ for the moving reference frame is obtained by approximating the time derivative $\partial\tilde{\mathbf{U}}_m/\partial t$ in Eq. (20) with a three point backward implicit formulation and is equal to:

$$\mathcal{L}_m^{MR}(\tilde{\mathbf{U}}_m, \tilde{\mathbf{U}}_m^n, \tilde{\mathbf{U}}_m^{n-1}) = \mathcal{R}_m^{MR}(\tilde{\mathbf{U}}_h) - \left[M(K_j^{(1)})\right]\left(\tfrac{3}{2}\tilde{\mathbf{U}}_m - 2\tilde{\mathbf{U}}_m^n + \tfrac{1}{2}\tilde{\mathbf{U}}_m^{n-1}\right)/\triangle t,$$

with $\mathcal{R}_m^{MR}$ defined in Eq. (20). It is important to note that the mass matrices $[M]$ for each element are uncoupled from the other elements and have a size of 5×5 for the space-time DG finite element method and 4×4 for the MRDG finite element method and can therefore be easily inverted when necessary.

The main difference with the commonly used definition of the pseudo-time equations is the multiplication of the pseudo-time derivative with the mass matrix $[M]$. The weighting of the

pseudo-time derivative with the mass matrix has as benefit that the equations for the flow field moments are solved instead of the expansion coefficients $\tilde{\mathbf{U}}_m$ for the flow field. For each implicit time step the mass matrix $[M]$ is constant when the evolution equations, given by Eq. (31), are marched to steady state in pseudo-time and this can be used to define the flow field moments $\tilde{\mathbf{W}}_m$ as:

$$\tilde{\mathbf{W}}_m = [M]\, \tilde{\mathbf{U}}_m.$$

Here the coefficient $\tilde{\mathbf{W}}_0$ is equal to the element average of the flow field multiplied with the element volume, see Eq. (26). The formulation using the flow field moments $\tilde{\mathbf{W}}_m$ results in much less coupling between the different equations in Eq. (31) than if the equations for the element expansion coefficients $\tilde{\mathbf{U}}_m$ are solved directly, because this requires the multiplication of $\mathcal{L}_m^{ST}$ and $\mathcal{L}_m^{MR}$ with $[T]^{-1}$ and $[M]^{-1}$, respectively. Inspection of the operators $\mathcal{R}_m^{ST}$ and $\mathcal{R}_m^{MR}$ shows that there is only a weak coupling between the different components. The main coupling is through the calculation of the left and right states in the Riemann problem, which is part of the flux calculation, and depends on $\bar{\mathbf{U}}_h^{int(\mathcal{K})}$ and $\bar{\mathbf{U}}_h^{ext(\mathcal{K})}$, which are a linear combination of the expansion coefficients $\tilde{\mathbf{U}}_m$, Eqs. (23)-(24).

The loose coupling between the equations for $\tilde{\mathbf{W}}_m$ is important for the multigrid scheme, because it makes it possible to solve only equations for $\tilde{\mathbf{W}}_0$ on the coarse grid and discard the other flow field moments on the coarse grids. This means that on the coarse grids only the equations for the element averaged flow field are solved, resulting in a significant simplification in the multigrid algorithm. This could not be accomplished by simply using equations for $\tilde{\mathbf{U}}_0$, because this coefficient is strongly coupled to the other expansion coefficients and on non-rectangular elements $\tilde{\mathbf{U}}_0$ is not equal to the element average of the flow field variables.

The use of a second-order accurate discretization on the coarse grids has also been tested, but this did not result in an efficient multigrid algorithm because the slope limiter produced a significant amount of high frequency disturbances on the coarse grids, which causes a degradation of convergence. Also the restriction and prolongation operators for a second-order accurate discretization on the coarse grids are considerably more complicated, because the flow field expansion coefficients must be calculated by projecting the fine grid flow field onto the coarse grid elements, which is a non-trivial problem on general unstructured meshes.

The multigrid scheme uses the TVD Runge-Kutta time integration method from Shu and Osher [19] as relaxation scheme. These Runge-Kutta schemes are stable for CFL numbers less than one, but all calculations discussed in this paper have been done using a CFL number of 0.7 and the third

order TVD Runge-Kutta scheme. The Runge-Kutta scheme is combined with the slope limiting procedure which is applied each Runge-Kutta stage.

The calculation of the flow field at a new implicit time level $t = (n+1)\triangle t$ using the FAS multigrid scheme can now be obtained by the following steps:

- *Calculate at pseudo-time level $\tau = 0$ on the fine grid with index $l = L$ the flow field moments:*

$$\tilde{\mathbf{W}}_m^{L,0} = [M]\,\tilde{\mathbf{U}}_m^n, \qquad m \in \{0, \cdots, M_G\}.$$

- *Solve Eq. (31) for the expansion coefficients $\tilde{\mathbf{W}}_m^{l,k}$ with index $m \in \{0, \cdots, M_G\}$ on the fine grid L and $m = 0$ on the coarse grids $l < L$ at each pseudo-time level $\tau = k\triangle\tau$, $(k = 0, 1, \cdots)$, using the TVD Runge-Kutta scheme in combination with a multigrid cycling strategy with grid levels $l \in \{1, \cdots, L\}$:*

$$\begin{aligned} \mathbf{V}_{mi}^{(0)} &= \mathbf{W}_{mi}^{l,k}, \\ (1+\gamma_s\bar{\lambda})\,\tilde{V}_{mi}^{(s)} &= \Pi_{mpi}\left(\alpha_s\tilde{V}_{pi}^{(0)} + (\beta_s+\gamma_s\bar{\lambda})\tilde{V}_{pi}^{(s-1)} + \gamma_s\triangle\tau(\mathcal{L}_{pi}^l(\tilde{\mathbf{V}}_m^{(s-1)}, \tilde{\mathbf{U}}_m^n, \tilde{\mathbf{U}}_m^{n-1}) + \mathcal{F}_{pi}^l)\right), \\ & \qquad\qquad \textit{for } s = 1, \cdots, S, \quad (32) \\ & \qquad\qquad i \in \{1, \cdots, 5\},\ \textit{no summation on } i. \end{aligned}$$

  Update the flow field moments:

$$\mathbf{W}_m^{l,k+1} = \tilde{\mathbf{V}}_m^{(S)},$$

  and continue to the next pseudo-time level until $\mathcal{L}_m^L(\tilde{\mathbf{V}}_m^L, \tilde{\mathbf{U}}_m^n, \tilde{\mathbf{U}}_m^{n-1}) < \epsilon$, with ϵ a predefined tolerance, or the maximum number of predefined pseudo-time steps is reached.

- *Advance to the next implicit time level and update:*

$$\tilde{\mathbf{U}}_m^{n+1} = [M]^{-1}\,\mathbf{W}_m^L.$$

Here l denotes the grid level with L the finest grid level, S the number of Runge-Kutta stages with stage index s and M_G is equal to four for the space-time DG method and three for the MRDG finite element method. The index k represents the pseudo-time index and i the flow field component. The coefficients α_s, β_s and γ_s of the TVD Runge-Kutta schemes are listed in Table 1. The limiting operator Π_{mpi}, defined in Eq. (30), depends on the unlimited flow field after each Runge-Kutta stage. The same corrections as proposed by Melson et al. [14] are applied to the Runge-Kutta

Order	Stages	α	β	γ
1	1	1	0	1
2	2	$\frac{3}{4}$	$\frac{1}{4}$	$\frac{1}{4}$
3	3	$\frac{1}{3}$	$\frac{2}{3}$	$\frac{2}{3}$

Table 1: Coefficients for TVD Runge-Kutta schemes from Shu and Osher [19]

scheme in Eq. (32). This results in a point implicit treatment of the linear contribution of the flow field moments $\tilde{\mathbf{W}}_m$ in the operator $\mathcal{L}_m$ which significantly enhances stability for small values of $\triangle t$. The variable $\bar{\lambda}$ is defined as $\bar{\lambda} = \frac{\triangle \tau}{\triangle t}$ for the space-time DG method, with $\triangle t$ the global time step, and $\bar{\lambda} = \frac{3\triangle \tau}{2\triangle t}$ for the discretization using a moving reference frame. The multigrid forcing function $\mathcal{F}^l$ is defined as:

$$\begin{aligned} \mathcal{F}_m^l &= \mathcal{L}_m^l(\mathcal{I}_{l+1}^l \tilde{\mathbf{U}}_m^{l+1}, \mathcal{I}_{l+1}^l \tilde{\mathbf{U}}_m^{l+1,n}, \mathcal{I}_{l+1}^l \tilde{\mathbf{U}}_m^{l+1,n-1}) + \mathcal{I}_{l+1}^l \left(\mathcal{F}_m^{l+1} - \mathcal{L}_m^{l+1} \right), && \text{if } l < L, \\ &= 0, && \text{if } l = L, \end{aligned}$$

with $\mathcal{I}_{l+1}^l$ the restriction operator from the grid at level $l+1$ to the next coarse grid level l. The contributions $\tilde{\mathbf{U}}_m^n$ and $\tilde{\mathbf{U}}_m^{n-1}$ do not change at the coarse grid levels and it is therefore not necessary to include them into the forcing function, saving the expense of calculating the restriction of these variables to the coarse grid, [14].

The restriction operator $\mathcal{I}_{l+1}^l$ for the space-time flow field moments is defined as:

$$\begin{aligned} \mathcal{I}_{l+1}^l \tilde{\mathbf{W}}_0^{l+1} &= \frac{\sum_{j=1}^{n_f} M_{0,m}^{l+1}(\mathcal{K}_j^{n+1}) \tilde{\mathbf{U}}_m^{l+1}}{\sum_{j=1}^{n_f} M_{0,0}^{l+1}(\mathcal{K}_j^{n+1})} && \text{if } l+1 = L, \\ &= \frac{\sum_{j=1}^{n_f} M_{0,0}^{l+1}(\mathcal{K}_j^{n+1}) \tilde{\mathbf{U}}_0^{l+1}}{\sum_{j=1}^{n_f} M_{0,0}^{l+1}(\mathcal{K}_j^{n+1})} && \text{if } l+1 < L, \end{aligned}$$

with n_f the number of elements at the fine grid level $l+1$ which are contained in the element at the coarse grid level l. A similar relation is used for the MRDG finite element method, but with $\mathcal{K}_j^{n+1}$ replaced by $K_j^{(1)}$. The prolongation operator $\mathcal{I}_l^{l+1}$ is a simple injection.

The update of the fine grid data with the coarse grid solution in the multigrid procedure is done with the relation:

$$\tilde{\mathbf{W}}_0^{l+1} = \tilde{\mathbf{W}}_0^{l+1} + \mathcal{I}_l^{l+1}(\tilde{\mathbf{W}}_0^l - \mathcal{I}_{l+1}^l \tilde{\mathbf{W}}_0^{l+1}). \tag{33}$$

If the grid level $l+1 < L$ then only the mean flow field $\tilde{\mathbf{W}}_0$ is corrected, but on the finest grid level when $l+1 = L$, first a corrected expansion coefficient $\tilde{\mathbf{W}}_0^{*L}$ is calculated using Eq. (33), after which new fine grid expansion coefficients are obtained by solving the following set of linear equations for $\tilde{\mathbf{U}}_m^L$:

$$M_{nm}^L \tilde{U}_{mi}^L = \begin{pmatrix} \tilde{W}_{0,i}^{*L} \\ \tilde{W}_{1,i}^{L} \\ \vdots \\ \tilde{W}_{M_G,i}^{L} \end{pmatrix}, \qquad i \in \{1, \cdots, 5\},$$

with M_G the number of expansion coefficients used to describe the flow field.

7 Discussion and Results

The two formulations of the discontinuous Galerkin finite element method for time-dependent calculations with dynamic grid motion presented in this paper are tested with simulations of a delta wing in pitching oscillation. These calculations serve three purposes. First they are used to verify the implementation of the two discretization techniques presented in this paper by conducting time-accurate simulations with sufficient accuracy such that it can be expected that both methods give nearly identical results. Secondly, this comparison is helpfull to get insight into the performance of both methods. The third objective is to investigate the capability of both inviscid methods in simulating time-dependent vortical flow about a sharp edged delta wing by comparing the simulation results with experiments. This information is important to aerospace industry because the simulation of unsteady viscous flow for complex aerodynamic configurations still requires large computational resources, especially when coupled with structural deformations.

The geometry of the delta wing is a cropped-delta wing with a 65-degree sweep angle and a sharp leading edge. The geometry in the calculations is limited to one half of the full geometry, Fig. 2, because only a pitching motion is simulated, and the flow field is considered symmetrical about the symmetry plane. A constant airfoil section in the streamwise direction is used (modified NACA 64A005 profile; straight line aft of 75% chord) with 5% relative thickness. More information about the geometry can be found in Elsenaar et al. [6]. The delta wing is subjected to a pitching motion around a point at $x_m = 0.5625$ and $z_m = -0.042$ in the centerline. Here the distances are made dimensionless with the inner chord length c_i^* of the delta wing. For a definition of the coordinate systems, see Fig. 3. The mean angle of attack $\bar{\alpha}$ is 9 degrees and the oscillation amplitude $\triangle\alpha$ is

12 degrees. The free stream Mach number in the calculations is $M_\infty = 0.4$. The reduced frequency of the oscillation $\omega = c_i^* \omega^* / U_\infty^*$ is 1.12, with ω^* and U_∞^*, the frequency and free stream velocity, respectively.

The grid used in the calculations with the MRDG finite element method, which uses a moving reference frame, consists of 245,760 elements and was initially generated as a block-structured grid and subsequently translated into the unstructured data format described in van der Vegt and van der Ven [25]. For the calculations with the space-time DG finite element method two grids are used with the same grid topology as used for the calculations with the moving reference frame. One grid with the grid coordinates at time level t_n and a second grid with the coordinates at time level t_{n+1}, which is obtained by transforming the grid at $t = t_n$ to the position and orientation of the delta wing at $t = t_{n+1}$. Three multigrid levels are used in the calculations, which are defined by omitting every other grid point from the initial structured fine grid. The non-linear equations for the implicit time integration methods are solved using a FAS multigrid scheme with a V-cycling strategy. Each implicit time step consists of 50 pseudo-time steps. During each pseudo-time step one full FAS multigrid cycle, with one pre- and one post-relaxation step on the fine grid level, is made. The number of pre- and post-relaxation steps on the coarse grids is doubled on each next coarser grid level.

The simulations are done with 20 and 40 time steps per cycle in order to investigate the effects of time step and its influence on forces, moments and pressure distribution. The simulations are started by first calculating a steady mean flow at the mean oscillation amplitude, but with angular velocity equal to zero. This effectively limits the transient time to one cycle and the simulations are run for a total of three full periods.

The results are compared with experiments done by Löser [13] in the Low Speed Wind tunnel DNW-NWB located at DLR Braunschweig. The delta wing geometry used in the experiments is slightly different from the geometry used in the calculations. The main difference is that the body and support are omitted in the calculations. This has some effect on the position of the main vortex, which is closer to the leading edge when the body is absent, especially close to the apex, but the influence is small in most parts of the flow field above the wing. The wind tunnel model of the delta wing was equipped with a large number of pressure transducers in cross-sections at $x_m = 0.3$, 0.6 and 0.8, both at the windward and leeward side of the model. The model also contained a balance for the measurement of forces and moments. The experiments considered pitch, roll and yaw oscillations, but the present study is limited to pitching oscillations only.

The free stream Mach number in the experiments was $M_\infty = 0.06$, which resulted in a Reynolds number of $Re = 1.55 * 10^6$ for a model with inner chord length $c_i^* = 1200$ mm. The free stream Mach number in the calculations is set equal to $M_\infty = 0.4$, which is significantly higher than the free stream Mach number in the experiments. The main reason for the use of a higher Mach number in the calculations is that the Mach number in the experiments is below the limit attainable by compressible Euler codes without special preconditioning to equilibriate the speed of sound and the convective velocity. The large discrepancy between these two velocities at low Mach numbers results in loss of accuracy and convergence problems. The use of the experimental Mach number would also result in an increased flow simulation time of at least a factor of five, which is considered unnecessary for this study. The use of a higher Mach number in the calculations has some influence on the results, but steady calculations at a Mach number of 0.2 showed that this was primarily limited to the vortex core, where the Mach number tends to be overpredicted in Euler simulations on a sufficiently fine grid due to the neglect of viscosity.

The pressure, force and moment data are Fourier analyzed and are presented in Löser [13] as amplitude and phase for the different harmonic components. Confidence intervals for amplitude and phase were obtained with an Analysis of Variance technique (ANOVA). The analysis of the experimental results of Löser [13] showed that only three harmonics are relevant to reproduce the signals and the results discussed in this paper are therefore limited to the same number of harmonics. The phase of the third harmonic could, however, not be measured with statistically significant accuracy and is therefore omitted from the results. After calculating the real ($\Re_n$) and imaginary ($\Im_n$) parts for the modes with index n using a Fast Fourier Transform (FFT) the results of both the experiments and calculations are transformed into an amplitude m_n and phase ϕ_n for each mode with index n using the following definition:

$$\Re_n \cos(n\omega t) - \Im_n \sin(n\omega t) = m_n \cos\left(n(\omega t + \phi_n)\right),$$

with:

$$\begin{aligned} m_n &= \sqrt{\Re_n^2 + \Im_n^2}, \\ \phi_n &= \arctan(\Im_n / \Re_n)/n. \end{aligned}$$

The signals then can be represented as:

$$m(t) = m_0 + \sum_{n=1}^{3} m_n \cos\left(n(\omega t + \phi_n)\right).$$

An important question for time-accurate simulations is the number of subiterations necessary to preserve time-accuracy when a pseudo-time formulation is used to solve the non-linear equations of the implicit time integration methods. Also a good performance of the multigrid convergence acceleration scheme is crucial for obtaining an efficient time integration method. In order to maintain time-accuracy it is not necessary to converge the residual every implicit time step to machine accuracy, but the error in the time integration should not be larger than the error caused by the spatial discretization. Since it is difficult to determine the number of subiterations from the absolute value of the residual it was decided to determine the number of subiterations from the convergence of the force and moments coefficients and performing the simulations with 20 and 40 time steps a period and investigate the effects of time step on the pressure coefficient distribution on the wing surface. Figures 4 and 5 show the evolution of the lift force coefficient during one implicit time step. Results are shown for both the MRDG and STDG finite element methods, with and without multigrid convergence acceleration. It is clear that the use of multigrid results in a significant improvement in convergence and about four to five times the number of work units is required to converge the force coefficients to the same level when no multigrid convergence acceleration is used. Here a work unit is defined as the amount of work necessary to do one pseudo-time step on the fine grid without using the multigrid scheme. One pseudo-time step using the multigrid scheme is 1.1 work units. During the simulations the evolution of the force and moments coefficients was monitored and it was concluded that 50 pseudo-time steps were sufficient for obtaining sufficiently converged results during each sub-iteration. The changes in the force and moment coefficients when the number of time steps during each oscillation period was changed from 40 to 20 are negligible. The effects of the number of time steps will be discussed more in detail when the Fourier modes of the pressure coefficient on the delta wing are discussed, because these coefficients are more sensitive to the accuracy of the flow solution.

Results of the measured and calculated lift, drag and pitching moment hysteresis curves, both for the STDG and the MRDG method, are shown in Figs. 6 through 8. The lift and drag coefficients C_L and C_D are defined as $C_L = L^*/(S^* U_\infty^*)$ and $C_D = D^*/(S^* U_\infty^*)$, respectively. Here L^* and D^* denote the lift and drag force and S^* the wing area. The pitching moment coefficient C_m is defined as $C_m = m^*/(S^* U_\infty^* c_i^*)$, with m^* the pitching moment. The moment reference point $\mathbf{x}_m$ is located at $\mathbf{x}_m = (0.5625, 0., 0.)$. The positive sense of force and moment coefficients is shown in Fig. 3.

The figures with the force and moment hysteresis curves show that both methods give nearly identical results, despite the significant differences in mathematical model. The only difference

is a shift in angle of attack which is caused by the difference in definition of time levels between the MRDG and STDG finite element methods which are shifted $\triangle t/2$. The hysteresis curves for the lift, drag and pitching moment coefficients show that there is a clear hysteresis effect. The amount of hysteresis in the lift and drag coefficients, relative to the steady results, is reasonably well predicted, but the curve for the lift coefficient is moved towards higher values in comparison with the experiments when the angle of attack increases. The prediction of the moment hysteresis curve is not as close and the whole curve is moved towards lower values. These results are typical for unsteady Euler simulations where the lift force generally is overpredicted due to the neglect of viscous effects, which are especially important in the vortex core. The differences between calculated and measured pitching moment coefficients can be partly explained due to the absence of secondary separation on the rear part of the delta wing, which is a purely viscous phenomenon and not present in the inviscid calculations.

The amplitudes and phases of both the calculated and measured first three Fourier harmonics of the pressure coefficient $-Cp$ at the locations $x_m = 0.6$ and 0.8 are presented in Figs. 9 through 20. Here the pressure coefficient is defined as $Cp = (p^* - p^*_\infty)/(\frac{1}{2}\rho_\infty U^{*2}_\infty)$, with p^* the pressure, ρ^* the density and the suffix ∞ refers to free stream values. Results are shown in Figs. 9 through 20 for both the MRDG and STDG finite element methods using 20 and 40 time steps per period. These figures show that both methods compare very well when 40 time steps per period are used, which gives confidence that both methods are properly implemented considering the significant differences in mathematical model between both methods. The dependence of the Fourier harmonics of the pressure coefficient $-Cp$ on the number of time steps per period increases with increasing mode index and is more important for the MRDG method. Comparing the results for the different number of time steps per period it can be concluded that the STDG finite element method is slightly more accurate in the calculation of the phase. The calculations of the amplitude of the pressure coefficient with the STDG method are slightly more dissipative in comparison with the MRDG method when the number of time steps per period is reduced. Figures 9 through 20 also show the error bands obtained with the ANOVA technique. A general conclusion from these error bands is that there is a significant phase error in the second mode.

The flow field about a delta wing is significantly influenced by a strong vortex at the leeward side of the delta wing. Depending on the Mach number and angle of attack complex structures of shocks and flow separation areas can occur. The discussion of the detailed physics of vortical flow about delta wings is beyond the scope of the present paper. More information can be found

in Narayan and Seshadri [15]. The present paper will concentrate on a discussion of the Fourier modes of the pressure coefficient on the upper and lower wing surface in order to verify and assess the capabilities of the MRDG and STDG finite element methods.

First the results at the windward side of the delta wing will be discussed. The Fourier modes m_0 of the pressure coefficient $-Cp$ at the lower wing surface at $x_m = 0.6$ and 0.8 are slightly shifted with respect to the measured results. The shift increases when moving more inboard where the body and sting were present in the experiment, which are omitted in the calculations. The amplitudes of the other modes and also the phase of the first mode are well predicted. There is no significant additional unsteadiness at the windward side of the delta wing during the pitching motion. This can be seen from the fact that the second and third mode amplitudes are rather small, except very close to the sharp leading edge. The pressure distribution at the windward side of the delta wing therefore quickly adjusts to the changes in angle of attack during the pitching oscillation for the circular frequency $\omega = 1.12$.

At the upper wing surface the calculated Fourier mode m_0 for the pressure coefficient $-Cp$ compares well with the experiment outside the region of the primary vortex. In the region where the flow field is dominated by a strong vortex, $y_m > 0.6$, the pressure coefficient is significantly overpredicted in the inviscid simulations in comparison with the experiments. This is a well known effect of neglecting the effects of viscosity. The effects of viscosity on the Fourier harmonics describing the unsteady flow field is, however, considerably less significant. At the leeward side of the delta wing there is a significant unsteady effect on the flow field due to the pitching motion, which is clear from amplitudes of the higher harmonics. The correlation of the amplitudes m_1, m_2 and m_3 is quite good, certainly when the limitations of an inviscid model are taken into account. The prediction of the phase of the first mode is good, but the correlation with the experiments for the phase of the higher is modes is not as good as for the amplitude. A general conclusion from the comparison between the simulation results and the experiments is that these simulations provide useful information about the unsteady flow field for delta wings in dynamic motion, provided that there is a good mechanism to generate vorticity into the inviscid flow field, such as a sharp leading edge.

The calculations were done on the NLR NEC SX-4 computer, which has 16 processors and 4 Gbyte main memory. The program is fully parallelized and vectorized and the calculations were run on seven processors reaching a speed of 3.4 Gflop/s. Seven processors were used because the simulations are not limited by turn-around time. The performance of the program for unsteady

calculations is not optimal yet, as the parallelized multigrid algorithm is not yet completely optimized, and the fact that the first order accurate discretization, used on the coarse grids, runs at a lower parallel efficiency. It should further be realized that the performance of time dependent simulations also depends on the significant amount of data analysis, which must be done during the simulations in order to prevent the storage of large data files, and the generation of plot data, which both cannot be parallelized and consist mostly of serial calculations.

The simulations with 40 time steps per period required 1.35 Gbyte of main memory and 7.2 hours for the MRDG finite element method and 1.45 Gbyte and 7.8 hours for the STDG method. The memory use is relatively high, but a detailed analysis of the memory use in the simulation program showed that a reduction of approximately 50% can be obtained by more efficiently storing the data in the coarse grid multigrid levels and limiting the amount of temporary storage used in the vectorization and parallelization of the flux calculations. The computing time of the present simulations can be reduced by limiting the number of sub-iterations in the implicit time integration method. For most applicitations tested approximately 35 sub-iterations were sufficient. An additional reduction in computing time, independent of the specific simulation, can be obtained by improving the performance of the simulation program. A detailed analysis of CPU time spend in the different parts of the program shows that a significant amount of computing time is used for calculating the slope limiter and the update of the element residuals with the calculated fluxes. These routines are completely vectorized and parallelized, and contain only 25 % of the total operation count, but consume 49 % of the total computing time on the NEC SX-4 due to memory bank conflicts. The performance of these routines can be significantly improved using the domain partitioning algorithm, discussed in Van der Ven and Van der Vegt [27], and used to parallelize the grid adaptation part in the flow solver.

8 Concluding Remarks

A detailed analysis of a new space-time discontinuous Galerkin finite element method for the time-accurate simulation of inviscid compressible flows on dynamic, hexahedron type grids is presented. Also a more specialized discontinuous Galerkin method using moving reference frames is discussed. Both methods satisfy the geometric conservation law, which is crucial when dealing with dynamic grid motion, and have been successfully demonstrated with the simulation of unsteady compressible flows about a delta wing in pitching motion. An efficient technique for the calculation of the element

face fluxes is discussed and detailed information about the numerical models is provided. Special attention has been paid to the implicit time integration method and a FAS multigrid scheme is presented for the efficient solution of the non-linear equations resulting from the use of implicit time integration methods. Future work will concentrate on the coupling with aeroelastic codes and further enhancing the multigrid algorithm and parallel performance of the code and reducing memory use.

9 Acknowledgment

The advice and continued support of Dr. B. Oskam during the course of this project is greatly appreciated. Sincere thanks are due to Dr. H. van der Ven, who conducted a considerable part of the parallelization of the code, which significantly contributed to making the time-accurate simulations feasible. The permission of Mr. T. Löser and Prof. D. Hummel, TU Braunschweig to use their experimental data for comparison with the simulation results is greatfully acknowledged. This work was partially funded by the Netherlands Agency for Aerospace Programmes (NIVR) under contract 7601N.

References

[1] T.J. Barth and D.C. Jespersen, *The Design and Application of Upwind Schemes on Unstructured Meshes*, AIAA Paper 89-0366 (1989).

[2] C.L. Bottasso, On the computation of the boundary integral of space-time deforming finite elements, *Comm. in Numer. Methods in Engrg.* **13**, 53 (1997).

[3] B. Cockburn and C.-W. Shu, TVB Runge-Kutta local projection discontinuous Galerkin finite element method for conservation laws II: General framework, *Math. Comput.* **52**, 411 (1989).

[4] B. Cockburn, S.-Y. Lin and C.-W. Shu, TVD-Runge-Kutta local projection discontinuous Galerkin finite element method for conservation laws III: One-dimensional systems, *J. Comput. Phys.* **84**, 90 (1989).

[5] B. Cockburn, S. Hou and C.-W. Shu, The Runge-Kutta local projection discontinuous Galerkin finite element method for conservation laws IV: The multidimensional case, *Math. Comput.* **54**, 545 (1990).

[6] A. Elsenaar, L. Hjelmberg, K.A. Bütefisch and W.J. Bannink, The international vortex flow experiment, in *Proc. AGARD Symposium on Validation of Computational Fluid Dynamics, Lisbon, Portugal*, AGARD CP 437 (1987), also AGARD Advisory Report 303 (1994).

[7] K. Eriksson and C. Johnson, Adaptive finite element methods for parabolic problems V: long-time integration, *SIAM J. Numer. Anal.* **32**, 1750 (1995).

[8] P. Hansbo, Aspects of conservation in finite element flow computations, *Comput. Methods Appl. Mech. Engrg.* **117**, 423 (1994).

[9] P. Hansbo and C. Johnson, *Streamline Diffusion Finite Element Methods for Fluid Flow*, in Von Karman Institute for Fluid Dynamics, Lecture Series 1995-02 (1995).

[10] A. Harten and J.M. Hyman, Self adjusting grid methods for one-dimensional hyperbolic conservation laws, *J. Comput. Phys.* **50**, 235 (1983).

[11] A. Jameson, *Time Dependent Calculations using Multigrid, with Applications to Unsteady Flows past Airfoils and Wings*, AIAA Paper 91-1596 (1991).

[12] M. Lesoinne and C. Farhat, Geometric conservation laws for aeroelastic computations using unstructured dynamic meshes, in *Proc. AIAA CFD Conference, San Diego, California, 1995.* [AIAA Paper 95-1709-CP]

[13] T. Löser, *Dynamic Force and Pressure Measurements on an Oscillating Delta Wing at Low Speeds*, Report IB 129-96/9 DLR Braunschweig, (1996).

[14] N.D. Melson, M.D. Sanetrik and H.L. Atkins, Time-accurate Navier-Stokes calculations with multigrid acceleration, in *Proc. 6th Copper Mountain Confer. on Multigrid Methods* (1993).

[15] K.Y. Narayan and S.N. Seshadri, Types of flow on the lee side of delta wings, *Prog. Aerospace Sci.* **33**, 167 (1997).

[16] B. Nkonga and H. Guillard, Godunov type method on non-structured meshes for three-dimensional moving boundary problems, *Comput. Methods Appl. Mech. Engrg.*, **113**, 183 (1994).

[17] S. Osher and S. Chakravarthy, Upwind schemes and boundary conditions with applications to Euler equations in general geometries, *J. Comput. Phys.* **50**, 447 (1983).

[18] F. Shakib, T.J.R. Hughes and Z. Johan, A new finite element method for computational fluid dynamics: X. The compressible Euler and Navier-Stokes equations, *Comput. Methods Appl. Mech. Engrg.* **89**, 141 (1991).

[19] C.-W. Shu and S. Osher, Efficient implementation of essentially non-oscillatory shock-capturing schemes, *J. Comput. Phys.* **77**, 439 (1988).

[20] A.H. Stroud, *Approximate Calculation of Multiple Integrals* (Prentice-Hall, Englewood Cliffs, NJ, 1971).

[21] P.D. Thomas and C.K. Lombard, Geometric conservation law and its application to flow computations on moving grids, *AIAA J.* **17**, 1030 (1979).

[22] J.J.W. van der Vegt, *Higher-Order Accurate Osher Schemes with Application to Compressible Boundary Layer Stability*, AIAA Paper 93-3051 (1993).

[23] J.J.W. van der Vegt, Anisotropic grid refinement using an unstructured discontinuous Galerkin method for the three-dimensional Euler equations of gas dynamics, in *Proc. 12th AIAA CFD Conference, San Diego, California, 1995.* [AIAA Paper 95-1657-CP]

[24] J.J.W. van der Vegt and H. van der Ven, Hexahedron Based Grid Adaptation for Future Large Eddy Simulation, in *Proc. Progress and Challenges in CFD Methods and Algorithms, Seville, Spain, 1995.* [AGARD CP-578, p. 22-1]

[25] J.J.W. van der Vegt and H. van der Ven, Discontinuous Galerkin finite element method with anisotropic local grid refinement for inviscid compressible flows, *J. Comput. Phys.* **140**, 1 (1998).

[26] H. van der Ven and J.J.W. van der Vegt, Experiences with Advanced CFD Algorithms on NEC SX-4, in *Proc. Vector and Parallel Processing VECPAR '96*, edited by Palma and Dongarra, Lect. Notes in Computer Science, (Springer Verlag, 1997).

[27] H. van der Ven and J.J.W. van der Vegt, Partitioning and parallel development of an unstructured, adaptive flow solver on the NEC SX-4, to be published in *Proc. Parallel Computational Fluid Dynamics '97 Conference, Manchester, England, 1997.*

[28] V. Venkatakrishnan, Convergence to steady state solutions of the Euler equations on unstructured grids with limiters, *J. Comput. Phys.* **118**, 120 (1995).

[29] V. Venkatakrishnan and D.J. Mavriplis, Implicit method for the computation of unsteady flows on unstructured grids, *J. Comput. Phys.* **127**, 380 (1996).

A Appendix: Analytic Expressions for Metrical Coefficients

This Appendix describes the calculation of the metrical coefficients for the space-time discontinuous Galerkin method and the discontinuous Galerkin formulation using a moving reference frame. The basic elements are hexahedra K which are connected to the master element $\hat{K}$. The position of the faces and vertices of the master element $\hat{K}$ are shown in Fig. 1. The space-time elements $\mathcal{K}$ have subdomains $\mathcal{S}^i_{\mathcal{K}} = \cup_{t=t_n}^{t_{n+1}} e^i_K(t)$, where $e^i_K(t)$ is the face with index i of element K at time t, $i \in \{1, \cdots, 6\}$. The metrical coefficients are calculated using the mappings $F_{\mathcal{K}}$ and $F^{(1)}_K$, defined in Eqs. (5) and (18) respectively.

A.1 Space-Time Element Integrals

A.1.1 Element Face Moments

Define the vectors $\mathbf{a}^i_K$ and $\mathbf{b}^i_K$ as:

$$\mathbf{a}^i_K = \tfrac{1}{2}(\mathbf{x}^n_i(K) + \mathbf{x}^{n+1}_i(K)), \tag{34}$$

$$\mathbf{b}^i_K = \tfrac{1}{2}(\mathbf{x}^{n+1}_i(K) - \mathbf{x}^n_i(K)), \tag{35}$$

with $\mathbf{x}^n_i(K)$ and $\mathbf{x}^{n+1}_i(K)$ the vertices of element K at times $t = t_n$ and t_{n+1}. The integrals of the element face moments are equal to:

• Face with index 1:

$$\begin{aligned}
\int_{\mathcal{S}^1_{\mathcal{K}}} \phi_m \mathbf{n}\, dQ &= \sigma_0 \left(2(\mathbf{a}^1_K - \mathbf{a}^7_K) \times (\mathbf{a}^3_K - \mathbf{a}^5_K) + \tfrac{2}{3}(\mathbf{b}^1_K - \mathbf{b}^7_K) \times (\mathbf{b}^3_K - \mathbf{b}^5_K)\right), && m = 0,\\
&= \sigma_1 \left(2(\mathbf{a}^1_K - \mathbf{a}^7_K) \times (\mathbf{a}^3_K - \mathbf{a}^5_K) + \tfrac{2}{3}(\mathbf{b}^1_K - \mathbf{b}^7_K) \times (\mathbf{b}^3_K - \mathbf{b}^5_K)\right), && m = 1,\\
&= \sigma_2 \left(2(\mathbf{a}^5_K - \mathbf{a}^7_K) \times (\mathbf{a}^3_K - \mathbf{a}^1_K) + \tfrac{2}{3}(\mathbf{b}^5_K - \mathbf{b}^7_K) \times (\mathbf{b}^3_K - \mathbf{b}^1_K)\right), && m = 2,\\
&= \sigma_3 \left(2(\mathbf{a}^1_K - \mathbf{a}^5_K) \times (\mathbf{a}^7_K - \mathbf{a}^3_K) + \tfrac{2}{3}(\mathbf{b}^1_K - \mathbf{b}^5_K) \times (\mathbf{b}^7_K - \mathbf{b}^3_K)\right), && m = 3,\\
&= \sigma_4 \left((\mathbf{a}^1_K - \mathbf{a}^7_K) \times (\mathbf{b}^3_K - \mathbf{b}^5_K) + (\mathbf{b}^1_K - \mathbf{b}^7_K) \times (\mathbf{a}^3_K - \mathbf{a}^5_K)\right), && m = 4,
\end{aligned} \tag{36}$$

with $\sigma = (\frac{1}{4}, -\frac{1}{4}, \frac{1}{12}, \frac{1}{12}, \frac{1}{6})^T(t_{n+1} - t_n)$. The integrals $\int_{\mathcal{S}^2_{\mathcal{K}}} \phi_m \mathbf{n} dQ$ for a face with index 2 can be obtained by a simple permutation of the vectors $\mathbf{a}^i_K$ and $\mathbf{b}^i_K$ in Eq. (36): $1 \to 2$, $7 \to 8$, $3 \to 4$, $5 \to 6$ and using $\sigma = (\frac{1}{4}, \frac{1}{4}, \frac{1}{12}, \frac{1}{12}, \frac{1}{6})^T(t_{n+1} - t_n)$.

• Face with index 3:

$$\begin{aligned}
\int_{\mathcal{S}^3_{\mathcal{K}}} \phi_m \mathbf{n}\, dQ &= \sigma_0 \left(2(\mathbf{a}^1_K - \mathbf{a}^6_K) \times (\mathbf{a}^5_K - \mathbf{a}^2_K) + \tfrac{2}{3}(\mathbf{b}^1_K - \mathbf{b}^6_K) \times (\mathbf{b}^5_K - \mathbf{b}^2_K)\right), && m = 0,\\
&= \sigma_1 \left(2(\mathbf{a}^1_K - \mathbf{a}^2_K) \times (\mathbf{a}^6_K - \mathbf{a}^5_K) + \tfrac{2}{3}(\mathbf{b}^1_K - \mathbf{b}^2_K) \times (\mathbf{b}^6_K - \mathbf{b}^5_K)\right), && m = 1,\\
&= \sigma_2 \left(2(\mathbf{a}^1_K - \mathbf{a}^6_K) \times (\mathbf{a}^5_K - \mathbf{a}^2_K) + \tfrac{2}{3}(\mathbf{b}^1_K - \mathbf{b}^6_K) \times (\mathbf{b}^5_K - \mathbf{b}^2_K)\right), && m = 2,\\
&= \sigma_3 \left(2(\mathbf{a}^1_K - \mathbf{a}^5_K) \times (\mathbf{a}^2_K - \mathbf{a}^6_K) + \tfrac{2}{3}(\mathbf{b}^1_K - \mathbf{b}^5_K) \times (\mathbf{b}^2_K - \mathbf{b}^6_K)\right), && m = 3,\\
&= \sigma_4 \left((\mathbf{a}^1_K - \mathbf{a}^6_K) \times (\mathbf{b}^5_K - \mathbf{b}^2_K) + (\mathbf{b}^1_K - \mathbf{b}^6_K) \times (\mathbf{a}^5_K - \mathbf{a}^2_K)\right), && m = 4,
\end{aligned} \tag{37}$$

with $\sigma = (\frac{1}{4}, \frac{1}{12}, -\frac{1}{4}, \frac{1}{12}, \frac{1}{6})^T (t_{n+1} - t_n)$. The integrals $\int_{\mathcal{S}^4_{\mathcal{K}}} \phi_m \mathbf{n} dQ$ for a face with index 4 can be obtained by a simple permutation of the vectors $\mathbf{a}^i_K$ and $\mathbf{b}^i_K$ in Eq. (37): $1 \to 3$, $2 \to 4$, $5 \to 7$, $6 \to 8$ and using $\sigma = (\frac{1}{4}, \frac{1}{12}, \frac{1}{4}, \frac{1}{12}, \frac{1}{6})^T (t_{n+1} - t_n)$.

• Face with index 5:

$$\begin{aligned}
\int_{\mathcal{S}^5_{\mathcal{K}}} \phi_m \mathbf{n}\, dQ &= \sigma_0 \left(2(\mathbf{a}^1_K - \mathbf{a}^4_K) \times (\mathbf{a}^2_K - \mathbf{a}^3_K) + \tfrac{2}{3}(\mathbf{b}^1_K - \mathbf{b}^4_K) \times (\mathbf{b}^2_K - \mathbf{b}^3_K)\right), && m = 0,\\
&= \sigma_1 \left(2(\mathbf{a}^1_K - \mathbf{a}^2_K) \times (\mathbf{a}^3_K - \mathbf{a}^4_K) + \tfrac{2}{3}(\mathbf{b}^1_K - \mathbf{b}^2_K) \times (\mathbf{b}^3_K - \mathbf{b}^4_K)\right), && m = 1,\\
&= \sigma_2 \left(2(\mathbf{a}^1_K - \mathbf{a}^3_K) \times (\mathbf{a}^4_K - \mathbf{a}^2_K) + \tfrac{2}{3}(\mathbf{b}^1_K - \mathbf{b}^3_K) \times (\mathbf{b}^4_K - \mathbf{b}^2_K)\right), && m = 2,\\
&= \sigma_3 \left(2(\mathbf{a}^1_K - \mathbf{a}^4_K) \times (\mathbf{a}^2_K - \mathbf{a}^3_K) + \tfrac{2}{3}(\mathbf{b}^1_K - \mathbf{b}^4_K) \times (\mathbf{b}^2_K - \mathbf{b}^3_K)\right), && m = 3,\\
&= \sigma_4 \left((\mathbf{a}^1_K - \mathbf{a}^4_K) \times (\mathbf{b}^2_K - \mathbf{b}^3_K) + (\mathbf{b}^1_K - \mathbf{b}^4_K) \times (\mathbf{a}^2_K - \mathbf{a}^3_K)\right), && m = 4,
\end{aligned} \tag{38}$$

with $\sigma = (\frac{1}{4}, \frac{1}{12}, \frac{1}{12}, -\frac{1}{4}, \frac{1}{6})^T (t_{n+1} - t_n)$. The integrals $\int_{\mathcal{S}^6_{\mathcal{K}}} \phi_m \mathbf{n} dQ$ for a face with index 6 can be obtained by a simple permutation of the vectors $\mathbf{a}^i_K$ and $\mathbf{b}^i_K$ in Eq. (38): $1 \to 5$, $2 \to 6$, $3 \to 7$, $4 \to 8$ and using $\sigma = (\frac{1}{4}, \frac{1}{12}, \frac{1}{12}, \frac{1}{4}, \frac{1}{6})^T (t_{n+1} - t_n)$.

A.1.2 Element Face Velocity Moments

For efficiency reasons the element face velocity moments are expressed in terms of the element face moments defined in Appendix A.1.1.

• Face with index 1:

$$\begin{aligned}
\int_{\mathcal{S}^1_{\mathcal{K}}} \phi_m\, \mathbf{n}\cdot\mathbf{s}\, dQ &= \dot{\mathbf{b}}^1_K \cdot \int_{\mathcal{S}^1_{\mathcal{K}}} \phi_0 \mathbf{n} dQ + \dot{\mathbf{b}}^2_K \cdot \int_{\mathcal{S}^1_{\mathcal{K}}} \phi_2 \mathbf{n} dQ + \dot{\mathbf{b}}^3_K \cdot \int_{\mathcal{S}^1_{\mathcal{K}}} \phi_3 \mathbf{n} dQ, && m=0,\\
&= -\int_{\mathcal{S}^1_{\mathcal{K}}} \phi_0 \mathbf{n}\cdot\mathbf{s} dQ, && m=1,\\
&= \tfrac{1}{3}\dot{\mathbf{b}}^2_K \cdot \int_{\mathcal{S}^1_{\mathcal{K}}} \phi_0 \mathbf{n} dQ + \dot{\mathbf{b}}^1_K \cdot \int_{\mathcal{S}^1_{\mathcal{K}}} \phi_2 \mathbf{n} dQ + \tfrac{1}{3}\dot{\mathbf{b}}^4_K \cdot \int_{\mathcal{S}^1_{\mathcal{K}}} \phi_3 \mathbf{n} dQ, && m=2,\\
&= \tfrac{1}{3}\dot{\mathbf{b}}^3_K \cdot \int_{\mathcal{S}^1_{\mathcal{K}}} \phi_0 \mathbf{n} dQ + \tfrac{1}{3}\dot{\mathbf{b}}^4_K \cdot \int_{\mathcal{S}^1_{\mathcal{K}}} \phi_2 \mathbf{n} dQ + \dot{\mathbf{b}}^1_K \cdot \int_{\mathcal{S}^1_{\mathcal{K}}} \phi_3 \mathbf{n} dQ, && m=3,\\
&= \dot{\mathbf{b}}^1_K \cdot \int_{\mathcal{S}^1_{\mathcal{K}}} \phi_4 \mathbf{n} dQ + \\
&\quad \sigma_4 \dot{\mathbf{b}}^2_K \cdot \Big((\mathbf{a}^5_K - \mathbf{a}^7_K)\times(\mathbf{b}^3_K - \mathbf{b}^1_K) + (\mathbf{b}^5_K - \mathbf{b}^7_K)\times(\mathbf{a}^3_K - \mathbf{a}^1_K) \Big) + \\
&\quad \sigma_4 \dot{\mathbf{b}}^3_K \cdot \Big((\mathbf{a}^1_K - \mathbf{a}^5_K)\times(\mathbf{b}^7_K - \mathbf{b}^3_K) + (\mathbf{b}^1_K - \mathbf{b}^5_K)\times(\mathbf{a}^7_K - \mathbf{a}^3_K) \Big), && m=4.
\end{aligned} \tag{39}$$

• Face with index 3:

$$\begin{aligned}
\int_{\mathcal{S}^3_{\mathcal{K}}} \phi_m\, \mathbf{n}\cdot\mathbf{s}\, dQ &= \dot{\mathbf{b}}^1_K \cdot \int_{\mathcal{S}^3_{\mathcal{K}}} \phi_0 \mathbf{n} dQ + \dot{\mathbf{b}}^2_K \cdot \int_{\mathcal{S}^3_{\mathcal{K}}} \phi_1 \mathbf{n} dQ + \dot{\mathbf{b}}^3_K \cdot \int_{\mathcal{S}^3_{\mathcal{K}}} \phi_3 \mathbf{n} dQ, && m=0,\\
&= \tfrac{1}{3}\dot{\mathbf{b}}^2_K \cdot \int_{\mathcal{S}^3_{\mathcal{K}}} \phi_0 \mathbf{n} dQ + \dot{\mathbf{b}}^1_K \cdot \int_{\mathcal{S}^3_{\mathcal{K}}} \phi_1 \mathbf{n} dQ + \tfrac{1}{3}\dot{\mathbf{b}}^4_K \cdot \int_{\mathcal{S}^3_{\mathcal{K}}} \phi_3 \mathbf{n} dQ, && m=1,\\
&= -\int_{\mathcal{S}^3_{\mathcal{K}}} \phi_0 \mathbf{n}\cdot\mathbf{s} dQ, && m=2,\\
&= \tfrac{1}{3}\dot{\mathbf{b}}^3_K \cdot \int_{\mathcal{S}^3_{\mathcal{K}}} \phi_0 \mathbf{n} dQ + \tfrac{1}{3}\dot{\mathbf{b}}^4_K \cdot \int_{\mathcal{S}^3_{\mathcal{K}}} \phi_1 \mathbf{n} dQ + \dot{\mathbf{b}}^1_K \cdot \int_{\mathcal{S}^3_{\mathcal{K}}} \phi_3 \mathbf{n} dQ, && m=3,\\
&= \dot{\mathbf{b}}^1_K \cdot \int_{\mathcal{S}^3_{\mathcal{K}}} \phi_4 \mathbf{n} dQ + \\
&\quad \sigma_4 \dot{\mathbf{b}}^2_K \cdot \Big((\mathbf{a}^1_K - \mathbf{a}^2_K)\times(\mathbf{b}^6_K - \mathbf{b}^5_K) + (\mathbf{b}^1_K - \mathbf{b}^2_K)\times(\mathbf{a}^6_K - \mathbf{a}^5_K) \Big) + \\
&\quad \sigma_4 \dot{\mathbf{b}}^3_K \cdot \Big((\mathbf{a}^1_K - \mathbf{a}^5_K)\times(\mathbf{b}^2_K - \mathbf{b}^6_K) + (\mathbf{b}^1_K - \mathbf{b}^5_K)\times(\mathbf{a}^2_K - \mathbf{a}^6_K) \Big), && m=4.
\end{aligned} \tag{40}$$

• Face with index 5:

$$
\begin{aligned}
\int_{\mathcal{S}^5_{\mathcal{K}}} \phi_m \, \mathbf{n}\cdot\mathbf{s}\, dQ &= \dot{\mathbf{b}}^1_K \cdot \int_{\mathcal{S}^5_{\mathcal{K}}} \phi_0 \mathbf{n} dQ + \dot{\mathbf{b}}^2_K \cdot \int_{\mathcal{S}^5_{\mathcal{K}}} \phi_1 \mathbf{n} dQ + \dot{\mathbf{b}}^3_K \cdot \int_{\mathcal{S}^5_{\mathcal{K}}} \phi_2 \mathbf{n} dQ, && m=0,\\
&= \tfrac{1}{3}\dot{\mathbf{b}}^2_K \cdot \int_{\mathcal{S}^5_{\mathcal{K}}} \phi_0 \mathbf{n} dQ + \dot{\mathbf{b}}^1_K \cdot \int_{\mathcal{S}^5_{\mathcal{K}}} \phi_1 \mathbf{n} dQ + \tfrac{1}{3}\dot{\mathbf{b}}^4_K \cdot \int_{\mathcal{S}^5_{\mathcal{K}}} \phi_2 \mathbf{n} dQ, && m=1,\\
&= \tfrac{1}{3}\dot{\mathbf{b}}^3_K \cdot \int_{\mathcal{S}^5_{\mathcal{K}}} \phi_0 \mathbf{n} dQ + \tfrac{1}{3}\dot{\mathbf{b}}^4_K \cdot \int_{\mathcal{S}^5_{\mathcal{K}}} \phi_1 \mathbf{n} dQ + \dot{\mathbf{b}}^1_K \cdot \int_{\mathcal{S}^5_{\mathcal{K}}} \phi_2 \mathbf{n} dQ, && m=2,\\
&= -\int_{\mathcal{S}^5_{\mathcal{K}}} \phi_0 \mathbf{n}\cdot\mathbf{s} dQ, && m=3,\\
&= \dot{\mathbf{b}}^1_K \cdot \int_{\mathcal{S}^5_{\mathcal{K}}} \phi_4 \mathbf{n} dQ + \\
&\quad \sigma_4 \dot{\mathbf{b}}^2_K \cdot \Big((\mathbf{a}^1_K - \mathbf{a}^2_K)\times(\mathbf{b}^3_K - \mathbf{b}^4_K) + (\mathbf{b}^1_K - \mathbf{b}^2_K)\times(\mathbf{a}^3_K - \mathbf{a}^4_K) \Big) + \\
&\quad \sigma_4 \dot{\mathbf{b}}^3_K \cdot \Big((\mathbf{a}^1_K - \mathbf{a}^3_K)\times(\mathbf{b}^4_K - \mathbf{b}^2_K) + (\mathbf{b}^1_K - \mathbf{b}^3_K)\times(\mathbf{a}^4_K - \mathbf{a}^2_K) \Big), && m=4,
\end{aligned}
\tag{41}
$$

with $\sigma_4 = \frac{1}{18}(t_{n+1} - t_n)$ The integrals $\int_{\mathcal{S}^{2p}_{\mathcal{K}}} \phi_m \mathbf{n}\cdot\mathbf{s} dQ$, $p \in \{1,2,3\}$ are identical to $\int_{\mathcal{S}^{2p+1}_{\mathcal{K}}} \phi_m \mathbf{n}\cdot\mathbf{s} dQ$ except for the coefficients $\dot{\mathbf{b}}^i_K$ and a change of sign for the equations $m = p$. The coefficients $\dot{\mathbf{b}}^i_K$ for a face with index 1 are related to the velocity of the four vertices of the element face and are defined as:

$$
\begin{aligned}
\dot{\mathbf{b}}^1_K &= \tfrac{1}{2}(\mathbf{b}^1_K + \mathbf{b}^3_K + \mathbf{b}^5_K + \mathbf{b}^7_K)/(t_{n+1} - t_n),\\
\dot{\mathbf{b}}^2_K &= \tfrac{1}{2}(\mathbf{b}^3_K - \mathbf{b}^1_K - \mathbf{b}^5_K + \mathbf{b}^7_K)/(t_{n+1} - t_n),\\
\dot{\mathbf{b}}^3_K &= \tfrac{1}{2}(\mathbf{b}^5_K - \mathbf{b}^1_K + \mathbf{b}^7_K - \mathbf{b}^3_K)/(t_{n+1} - t_n),\\
\dot{\mathbf{b}}^4_K &= \tfrac{1}{2}(\mathbf{b}^1_K - \mathbf{b}^3_K - \mathbf{b}^5_K + \mathbf{b}^7_K)/(t_{n+1} - t_n),
\end{aligned}
$$

with the coeffcients $\mathbf{b}^i_K$ defined in Eq. (35). The integrals for the other faces can be determined using the permutations of the coefficients $\mathbf{b}^i_K$: $1 \to 2$, $3 \to 4$, $5 \to 6$, $7 \to 8$ for face 2; $3 \to 2$, $7 \to 6$ for face 3; $1 \to 3$, $3 \to 4$, $5 \to 7$, $7 \to 8$ for face 4; $3 \to 2$, $5 \to 3$, $7 \to 4$ for face 5 and $1 \to 5$, $3 \to 6$, $5 \to 7$, $7 \to 8$ for face 6.

A.1.3 Volume Moments

The integrals $\int_{\hat{\mathcal{K}}} \mathbf{S}^n d^3\hat{x} d\tau$ can be expressed as:

$$\begin{aligned}
\int_{\hat{\mathcal{K}}} \mathbf{S}^1 d^3\hat{x} d\tau &= \tfrac{1}{2}(\mathbf{a}_K^3 + \mathbf{a}_K^4 - \mathbf{a}_K^5 - \mathbf{a}_K^6) \times (\mathbf{a}_K^7 + \mathbf{a}_K^8 - \mathbf{a}_K^1 - \mathbf{a}_K^2) + \\
&\quad \tfrac{1}{6}(\mathbf{b}_K^3 + \mathbf{b}_K^4 - \mathbf{b}_K^5 - \mathbf{b}_K^6) \times (\mathbf{b}_K^7 + \mathbf{b}_K^8 - \mathbf{b}_K^1 - \mathbf{b}_K^2) + \\
&\quad \tfrac{1}{6}(\mathbf{a}_K^1 - \mathbf{a}_K^2 - \mathbf{a}_K^7 + \mathbf{a}_K^8) \times (\mathbf{a}_K^3 - \mathbf{a}_K^4 - \mathbf{a}_K^5 + \mathbf{a}_K^6) + \\
&\quad \tfrac{1}{18}(\mathbf{b}_K^1 - \mathbf{b}_K^2 - \mathbf{b}_K^7 + \mathbf{b}_K^8) \times (\mathbf{b}_K^3 - \mathbf{b}_K^4 - \mathbf{b}_K^5 + \mathbf{b}_K^6) \\
\int_{\hat{\mathcal{K}}} \mathbf{S}^2 d^3\hat{x} d\tau &= \tfrac{1}{2}(\mathbf{a}_K^2 + \mathbf{a}_K^4 - \mathbf{a}_K^5 - \mathbf{a}_K^7) \times (\mathbf{a}_K^6 + \mathbf{a}_K^8 - \mathbf{a}_K^1 - \mathbf{a}_K^3) + \\
&\quad \tfrac{1}{6}(\mathbf{b}_K^2 + \mathbf{b}_K^4 - \mathbf{b}_K^5 - \mathbf{b}_K^7) \times (\mathbf{b}_K^6 + \mathbf{b}_K^8 - \mathbf{b}_K^1 - \mathbf{b}_K^3) + \\
&\quad \tfrac{1}{6}(\mathbf{a}_K^1 - \mathbf{a}_K^3 - \mathbf{a}_K^6 + \mathbf{a}_K^8) \times (\mathbf{a}_K^2 - \mathbf{a}_K^4 - \mathbf{a}_K^5 + \mathbf{a}_K^7) + \\
&\quad \tfrac{1}{18}(\mathbf{b}_K^1 - \mathbf{b}_K^3 - \mathbf{b}_K^6 + \mathbf{b}_K^8) \times (\mathbf{b}_K^2 - \mathbf{b}_K^4 - \mathbf{b}_K^5 + \mathbf{b}_K^7) \\
\int_{\hat{\mathcal{K}}} \mathbf{S}^3 d^3\hat{x} d\tau &= \tfrac{1}{2}(\mathbf{a}_K^2 + \mathbf{a}_K^6 - \mathbf{a}_K^3 - \mathbf{a}_K^7) \times (\mathbf{a}_K^4 + \mathbf{a}_K^8 - \mathbf{a}_K^1 - \mathbf{a}_K^5) + \\
&\quad \tfrac{1}{6}(\mathbf{b}_K^2 + \mathbf{b}_K^6 - \mathbf{b}_K^3 - \mathbf{b}_K^7) \times (\mathbf{b}_K^4 + \mathbf{b}_K^8 - \mathbf{b}_K^1 - \mathbf{b}_K^5) + \\
&\quad \tfrac{1}{6}(\mathbf{a}_K^1 - \mathbf{a}_K^4 - \mathbf{a}_K^5 + \mathbf{a}_K^8) \times (\mathbf{a}_K^2 - \mathbf{a}_K^3 - \mathbf{a}_K^6 + \mathbf{a}_K^7) + \\
&\quad \tfrac{1}{18}(\mathbf{b}_K^1 - \mathbf{b}_K^4 - \mathbf{b}_K^5 + \mathbf{b}_K^8) \times (\mathbf{b}_K^2 - \mathbf{b}_K^3 - \mathbf{b}_K^6 + \mathbf{b}_K^7). \qquad (42)
\end{aligned}$$

The coefficients $\mathbf{a}_K^i$ and $\mathbf{b}_K^i$ are defined in Eqs. (34)-(35).

A.2 Element Integrals for Moving Reference Frame

A.2.1 Element Face Rotation Moments

For efficiency reasons the results are expressed in terms of the element face moment integrals $\int_{e_K^i} \phi_m \mathbf{n} dS$, which are used to calculate the flux contribution not depending on the grid motion. Detailed expressions for the integrals $\int_{e_K^i} \phi_m \mathbf{n} dS$ can be found in Van der Vegt and Van der Ven [25]. In order to simplify notation the superscripts $^{(1)}$ are omitted in this section.

• Face with index 1:

$$\begin{aligned}
\int_{e_K^1} \phi_m \mathbf{r}\times\mathbf{n}dS &= \tfrac{1}{4}(\mathbf{a}_1\times\int_{e_K^1}\phi_0\mathbf{n}dS+\mathbf{a}_2\times\int_{e_K^1}\phi_2\mathbf{n}dS+\mathbf{a}_3\times\int_{e_K^1}\phi_3\mathbf{n}dS), && m=0,\\
&= -\int_{e_K^1}\phi_0\mathbf{r}\times\mathbf{n}dS, && m=1,\\
&= \tfrac{1}{4}\mathbf{a}_1\times\int_{e_K^1}\phi_2\mathbf{n}dS+\tfrac{1}{12}(\mathbf{a}_2\times\int_{e_K^1}\phi_0\mathbf{n}dS+\mathbf{a}_4\times\int_{e_K^1}\phi_3\mathbf{n}dS), && m=2,\\
&= \tfrac{1}{12}(\mathbf{a}_3\times\int_{e_K^1}\phi_0\mathbf{n}dS+\mathbf{a}_4\times\int_{e_K^1}\phi_2\mathbf{n}dS)+\tfrac{1}{4}\mathbf{a}_1\times\int_{e_K^1}\phi_3\mathbf{n}dS, && m=3,
\end{aligned}$$

with: (43)

$$\begin{aligned}
\mathbf{a}_1 &= \mathbf{x}_K^1+\mathbf{x}_K^3+\mathbf{x}_K^5+\mathbf{x}_K^7-4\mathbf{x}_b\\
\mathbf{a}_2 &= \mathbf{x}_K^3-\mathbf{x}_K^1+\mathbf{x}_K^7-\mathbf{x}_K^5\\
\mathbf{a}_3 &= \mathbf{x}_K^5-\mathbf{x}_K^1+\mathbf{x}_K^7-\mathbf{x}_K^3\\
\mathbf{a}_4 &= \mathbf{x}_K^1-\mathbf{x}_K^3-\mathbf{x}_K^5+\mathbf{x}_K^7,
\end{aligned}$$

and $\mathbf{x}_b$ the center of rotation in the moving reference system. The integrals $\int_{e_K^2}\phi_m\mathbf{r}\times\mathbf{n}dS$ for a face with index 2 can be obtained by a simple permutation of the vertices $\mathbf{x}_K^n$ in Eq. (43): $1\to 2$, $7\to 8$, $3\to 4$, $5\to 6$ and change of sign for $m=1$.

• Face with index 3:

$$\begin{aligned}
\int_{e_K^3} \phi_m \mathbf{r}\times\mathbf{n}dS &= \tfrac{1}{4}(\mathbf{a}_1\times\int_{e_K^3}\phi_0\mathbf{n}dS+\mathbf{a}_2\times\int_{e_K^3}\phi_1\mathbf{n}dS+\mathbf{a}_3\times\int_{e_K^3}\phi_3\mathbf{n}dS), && m=0,\\
&= \tfrac{1}{4}\mathbf{a}_1\times\int_{e_K^3}\phi_1\mathbf{n}dS+\tfrac{1}{12}(\mathbf{a}_2\times\int_{e_K^3}\phi_0\mathbf{n}dS+\mathbf{a}_4\times\int_{e_K^3}\phi_3\mathbf{n}dS), && m=1,\\
&= -\int_{e_K^3}\phi_0\mathbf{r}\times\mathbf{n}dS, && m=2,\\
&= \tfrac{1}{12}(\mathbf{a}_3\times\int_{e_K^3}\phi_0\mathbf{n}dS+\mathbf{a}_4\times\int_{e_K^3}\phi_1\mathbf{n}dS)+\tfrac{1}{4}\mathbf{a}_1\times\int_{e_K^3}\phi_3\mathbf{n}dS, && m=3,
\end{aligned}$$

with: (44)

$$\begin{aligned}
\mathbf{a}_1 &= \mathbf{x}_K^1+\mathbf{x}_K^2+\mathbf{x}_K^5+\mathbf{x}_K^6-4\mathbf{x}_b\\
\mathbf{a}_2 &= \mathbf{x}_K^2-\mathbf{x}_K^1+\mathbf{x}_K^6-\mathbf{x}_K^5\\
\mathbf{a}_3 &= \mathbf{x}_K^5-\mathbf{x}_K^1+\mathbf{x}_K^6-\mathbf{x}_K^2\\
\mathbf{a}_4 &= \mathbf{x}_K^1-\mathbf{x}_K^2+\mathbf{x}_K^6-\mathbf{x}_K^5.
\end{aligned}$$

The integrals $\int_{e_K^4}\phi_m\mathbf{r}\times\mathbf{n}dS$ for a face with index 4 can be obtained by a simple permutation of the vertices $\mathbf{x}_K^n$ in Eq. (44): $1\to 3$, $2\to 4$, $5\to 7$, $6\to 8$ and change of sign for $m=2$.

• Face with index 5:

$$\begin{aligned}
\int_{e_K^5} \phi_m \mathbf{r}\times\mathbf{n}dS &= \tfrac{1}{4}(\mathbf{a}_1\times\int_{e_k^5}\phi_0\mathbf{n}dS + \mathbf{a}_2\times\int_{e_K^5}\phi_1\mathbf{n}dS + \mathbf{a}_3\times\int_{e_K^5}\phi_2\mathbf{n}dS), && m=0,\\
&= \tfrac{1}{12}(\mathbf{a}_2\times\int_{e_K^5}\phi_0\mathbf{n}dS + \mathbf{a}_4\times\int_{e_k^5}\phi_2\mathbf{n}dS) + \tfrac{1}{4}\mathbf{a}_1\times\int_{e_K^5}\phi_1\mathbf{n}dS, && m=1,\\
&= \tfrac{1}{4}\mathbf{a}_1\times\int_{e_k^5}\phi_2\mathbf{n}dS + \tfrac{1}{12}(\mathbf{a}_3\times\int_{e_k^5}\phi_0\mathbf{n}dS + \mathbf{a}_4\times\int_{e_k^5}\phi_1\mathbf{n}dS), && m=2,\\
&= -\int_{e_k^5}\phi_0\mathbf{r}\times\mathbf{n}dS, && m=3,
\end{aligned} \tag{45}$$

with:

$$\begin{aligned}
\mathbf{a}_1 &= \mathbf{x}_K^1+\mathbf{x}_K^2+\mathbf{x}_K^3+\mathbf{x}_K^4-4\mathbf{x}_b\\
\mathbf{a}_2 &= \mathbf{x}_K^2-\mathbf{x}_K^1+\mathbf{x}_K^4-\mathbf{x}_K^3\\
\mathbf{a}_3 &= \mathbf{x}_K^3-\mathbf{x}_K^1+\mathbf{x}_K^4-\mathbf{x}_K^2\\
\mathbf{a}_4 &= \mathbf{x}_K^1-\mathbf{x}_K^2+\mathbf{x}_K^3+\mathbf{x}_K^4.
\end{aligned}$$

The integrals $\int_{e_K^6}\phi_m\mathbf{r}\times\mathbf{n}dS$ for a face with index 6 can be obtained by a simple permutation of the vertices $\mathbf{x}_K^n$ in Eq. (45): $1\to5$, $2\to6$, $3\to7$, $4\to8$ and change of sign for $m=3$.

A.2.2 Element Volume Rotation Moments

The calculation of the integrals for the element volume moments is greatly simplified by expressing the mapping $F_K^{(1)}$ for hexahedron elements, Eq. (18), as:

$$F_K^{(1)}:\mathbf{x}(\xi,\eta,\zeta)=\hat{\mathbf{x}}_K^1+\hat{\mathbf{x}}_K^2\xi+\hat{\mathbf{x}}_K^3\eta+\hat{\mathbf{x}}_K^4\zeta+\hat{\mathbf{x}}_K^5\xi\eta+\hat{\mathbf{x}}_K^6\xi\zeta+\hat{\mathbf{x}}_K^7\eta\zeta+\hat{\mathbf{x}}_K^8\xi\eta\zeta. \tag{46}$$

The coefficients $\hat{\mathbf{x}}_K^n=(\hat{x}_K^n,\hat{y}_K^n,\hat{z}_K^n)^T$ are obtained from the relation:

$$(\hat{x}_K^1,\cdots,\hat{x}_K^8)^T=A(x_K^1,\cdots,x_K^8)^T-\mathbf{b}^T x_b, \tag{47}$$

with $\mathbf{x}_b = (x_b, y_b, z_b)$ is the center of rotation in the moving reference system. The position of the element vertices $\mathbf{x}_K^n$ is indicated in Fig. 1. The matrix A is defined as:

$$A = \frac{1}{8}\begin{pmatrix} 1 & 1 & 1 & 1 & 1 & 1 & 1 & 1 \\ -1 & 1 & -1 & 1 & -1 & 1 & -1 & 1 \\ -1 & -1 & 1 & 1 & -1 & -1 & 1 & 1 \\ -1 & -1 & -1 & -1 & 1 & 1 & 1 & 1 \\ 1 & -1 & -1 & 1 & 1 & -1 & -1 & 1 \\ 1 & -1 & 1 & -1 & -1 & 1 & -1 & 1 \\ 1 & 1 & -1 & -1 & -1 & -1 & 1 & 1 \\ -1 & 1 & 1 & -1 & 1 & -1 & -1 & 1 \end{pmatrix},$$

and the vector $\mathbf{b}$ as:

$$\mathbf{b} = (1, 0, 0, 0, 0, 0, 0, 0)\,,$$

with identical relations for $\hat{y}_K^n$ and $\hat{z}_K^n$, with x in (47) replaced by y and z, respectively.

$$\begin{aligned}
\int_{\hat{K}} \mathbf{S}^1 \times \mathbf{r}\, d^3\hat{x} &= 8(\hat{\mathbf{x}}_K^3 \times \hat{\mathbf{x}}_K^4) \times \hat{\mathbf{x}}_K^1 + \tfrac{8}{3}\Big((\hat{\mathbf{x}}_K^3 \times \hat{\mathbf{x}}_K^6 + \hat{\mathbf{x}}_K^5 \times \hat{\mathbf{x}}_K^4) \times \hat{\mathbf{x}}_K^2 + \\
&\quad (\hat{\mathbf{x}}_K^5 \times \hat{\mathbf{x}}_K^6) \times \hat{\mathbf{x}}_K^1 + (\hat{\mathbf{x}}_K^3 \times \hat{\mathbf{x}}_K^7) \times \hat{\mathbf{x}}_K^3 + (\hat{\mathbf{x}}_K^7 \times \hat{\mathbf{x}}_K^4) \times \hat{\mathbf{x}}_K^4\Big) + \\
&\quad \tfrac{8}{9}\Big((\hat{\mathbf{x}}_K^5 \times \hat{\mathbf{x}}_K^8) \times \hat{\mathbf{x}}_K^3 + (\hat{\mathbf{x}}_K^8 \times \hat{\mathbf{x}}_K^6) \times \hat{\mathbf{x}}_K^4 + \\
&\quad (\hat{\mathbf{x}}_K^3 \times \hat{\mathbf{x}}_K^8 + \hat{\mathbf{x}}_K^5 \times \hat{\mathbf{x}}_K^7) \times \hat{\mathbf{x}}_K^5 + (\hat{\mathbf{x}}_K^7 \times \hat{\mathbf{x}}_K^6 + \hat{\mathbf{x}}_K^8 \times \hat{\mathbf{x}}_K^4) \times \hat{\mathbf{x}}_K^6\Big) \\
\int_{\hat{K}} \mathbf{S}^2 \times \mathbf{r}\, d^3\hat{x} &= 8(\hat{\mathbf{x}}_K^4 \times \hat{\mathbf{x}}_K^2) \times \hat{\mathbf{x}}_K^1 + \tfrac{8}{3}\Big((\hat{\mathbf{x}}_K^4 \times \hat{\mathbf{x}}_K^5 + \hat{\mathbf{x}}_K^7 \times \hat{\mathbf{x}}_K^2) \times \hat{\mathbf{x}}_K^3 + \\
&\quad (\hat{\mathbf{x}}_K^7 \times \hat{\mathbf{x}}_K^5) \times \hat{\mathbf{x}}_K^1 + (\hat{\mathbf{x}}_K^6 \times \hat{\mathbf{x}}_K^2) \times \hat{\mathbf{x}}_K^2 + (\hat{\mathbf{x}}_K^4 \times \hat{\mathbf{x}}_K^6) \times \hat{\mathbf{x}}_K^4\Big) + \\
&\quad \tfrac{8}{9}\Big((\hat{\mathbf{x}}_K^8 \times \hat{\mathbf{x}}_K^5) \times \hat{\mathbf{x}}_K^2 + (\hat{\mathbf{x}}_K^7 \times \hat{\mathbf{x}}_K^8) \times \hat{\mathbf{x}}_K^4 + \\
&\quad (\hat{\mathbf{x}}_K^6 \times \hat{\mathbf{x}}_K^5 + \hat{\mathbf{x}}_K^8 \times \hat{\mathbf{x}}_K^2) \times \hat{\mathbf{x}}_K^5 + (\hat{\mathbf{x}}_K^4 \times \hat{\mathbf{x}}_K^8 + \hat{\mathbf{x}}_K^7 \times \hat{\mathbf{x}}_K^6) \times \hat{\mathbf{x}}_K^7\Big) \\
\int_{\hat{K}} \mathbf{S}^3 \times \mathbf{r}\, d^3\hat{x} &= 8(\hat{\mathbf{x}}_K^2 \times \hat{\mathbf{x}}_K^3) \times \hat{\mathbf{x}}_K^1 + \tfrac{8}{3}\Big((\hat{\mathbf{x}}_K^2 \times \hat{\mathbf{x}}_K^7 + \hat{\mathbf{x}}_K^6 \times \hat{\mathbf{x}}_K^3) \times \hat{\mathbf{x}}_K^4 + \\
&\quad (\hat{\mathbf{x}}_K^6 \times \hat{\mathbf{x}}_K^7) \times \hat{\mathbf{x}}_K^1 + (\hat{\mathbf{x}}_K^2 \times \hat{\mathbf{x}}_K^5) \times \hat{\mathbf{x}}_K^2 + (\hat{\mathbf{x}}_K^5 \times \hat{\mathbf{x}}_K^3) \times \hat{\mathbf{x}}_K^3\Big) + \\
&\quad \tfrac{8}{9}\Big((\hat{\mathbf{x}}_K^6 \times \hat{\mathbf{x}}_K^8) \times \hat{\mathbf{x}}_K^2 + (\hat{\mathbf{x}}_K^8 \times \hat{\mathbf{x}}_K^7) \times \hat{\mathbf{x}}_K^3 + \\
&\quad (\hat{\mathbf{x}}_K^2 \times \hat{\mathbf{x}}_K^8 + \hat{\mathbf{x}}_K^6 \times \hat{\mathbf{x}}_K^5) \times \hat{\mathbf{x}}_K^6 + (\hat{\mathbf{x}}_K^5 \times \hat{\mathbf{x}}_K^7 + \hat{\mathbf{x}}_K^8 \times \hat{\mathbf{x}}_K^3) \times \hat{\mathbf{x}}_K^7\Big)\,. \qquad (48)
\end{aligned}$$

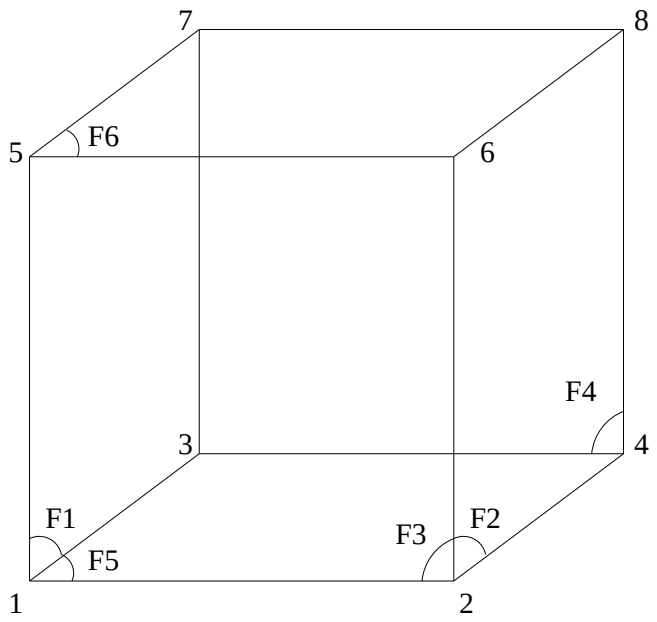

Figure 1: Face and vertex definition of master element $\hat{K}$.

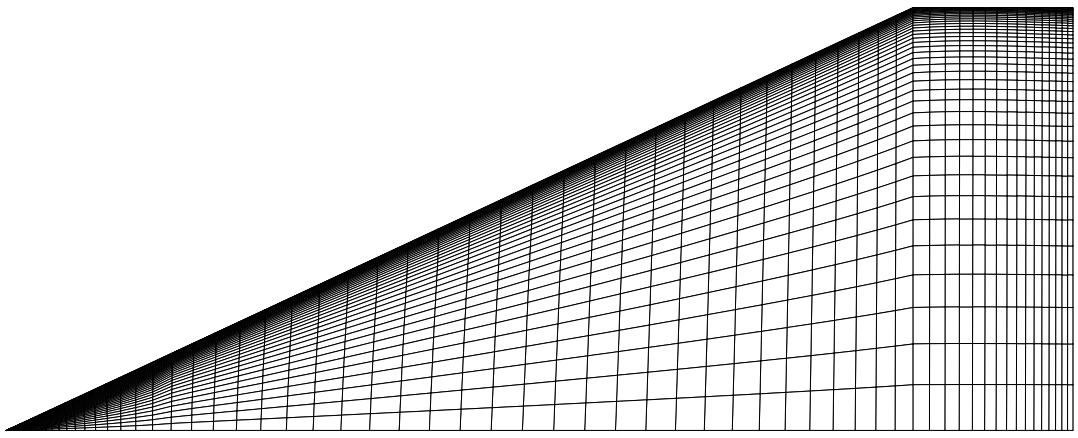

Figure 2: Delta wing geometry used in calculations (top view).

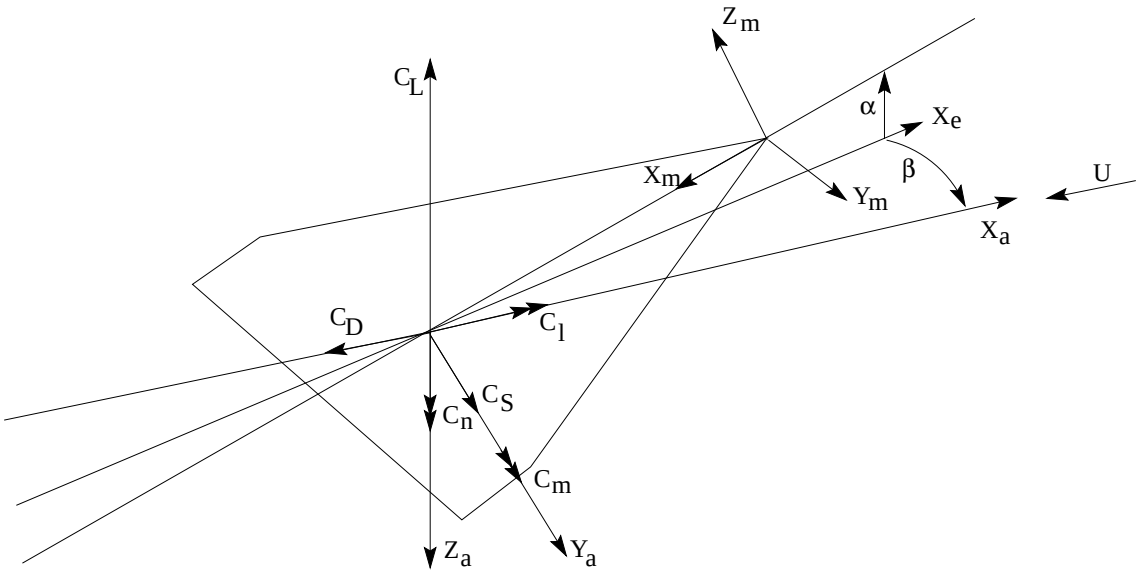

Figure 3: Coordinate systems and definition of reference system for forces and moments.

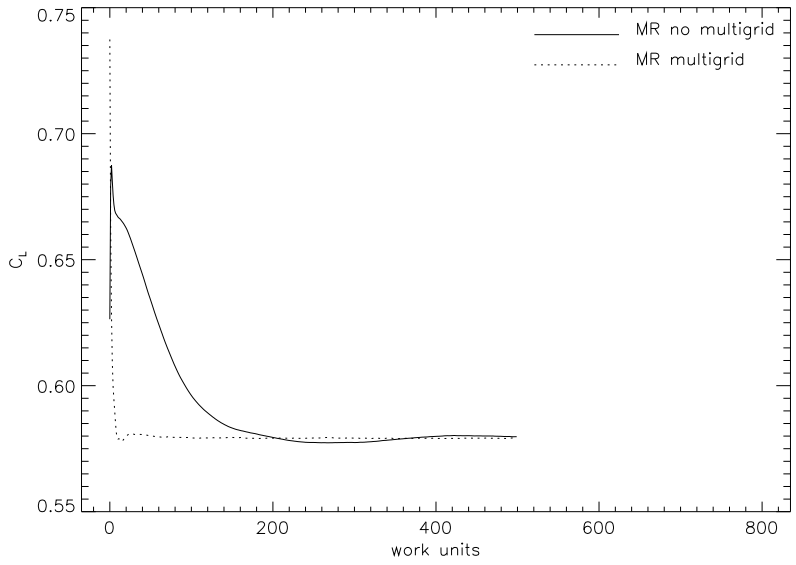

Figure 4: Evolution of lift force during one implicit time step for MRDG method with and without multigrid convergence acceleration.

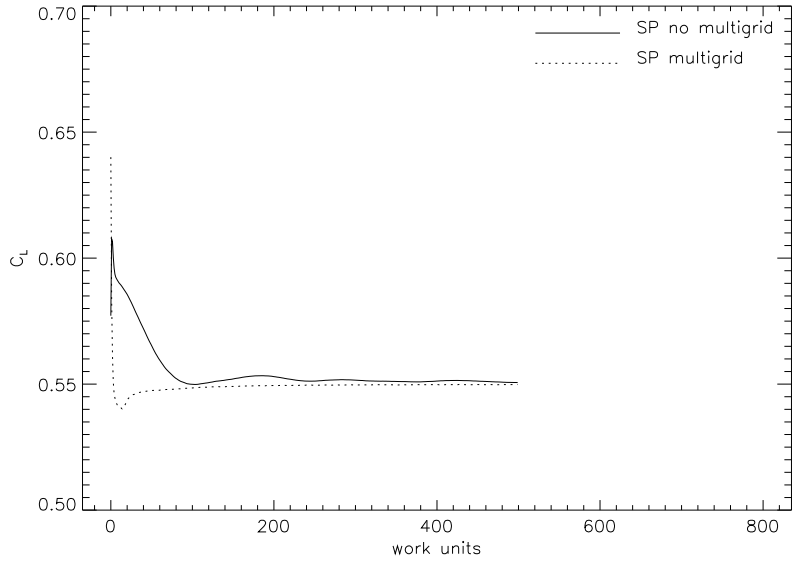

Figure 5: Evolution of lift force during one implicit time step for STDG method with and without multigrid convergence acceleration.

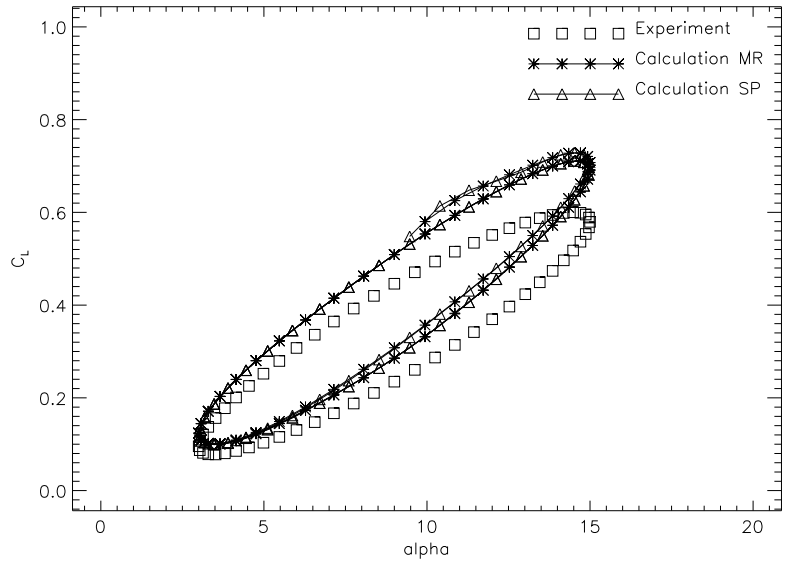

Figure 6: Lift hysteresis curve for delta wing in pitching motion ($\omega = 1.12$, $\bar{\alpha} = 9°$, $\triangle\alpha = 12°$, 3 periods with 40 time steps/period).

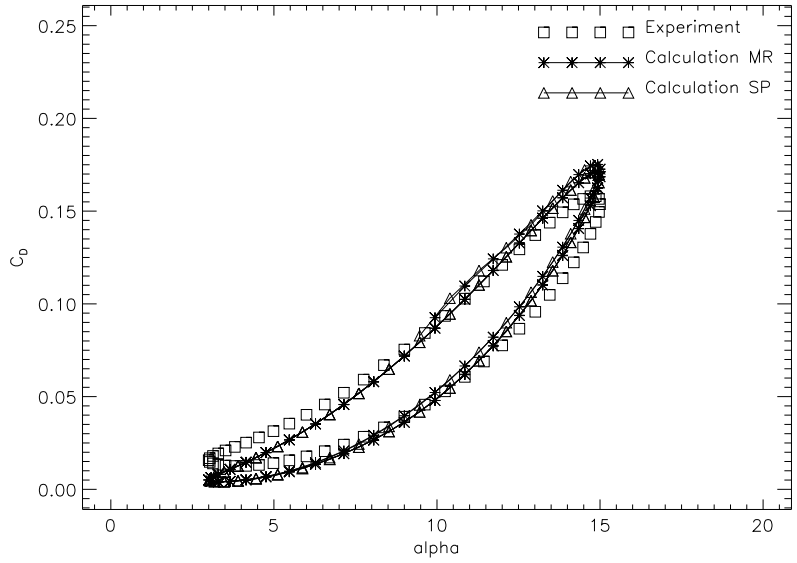

Figure 7: Drag hysteresis curve for delta wing in pitching motion ($\omega = 1.12$, $\bar{\alpha} = 9°$, $\triangle\alpha = 12°$, 3 periods with 40 time steps/period).

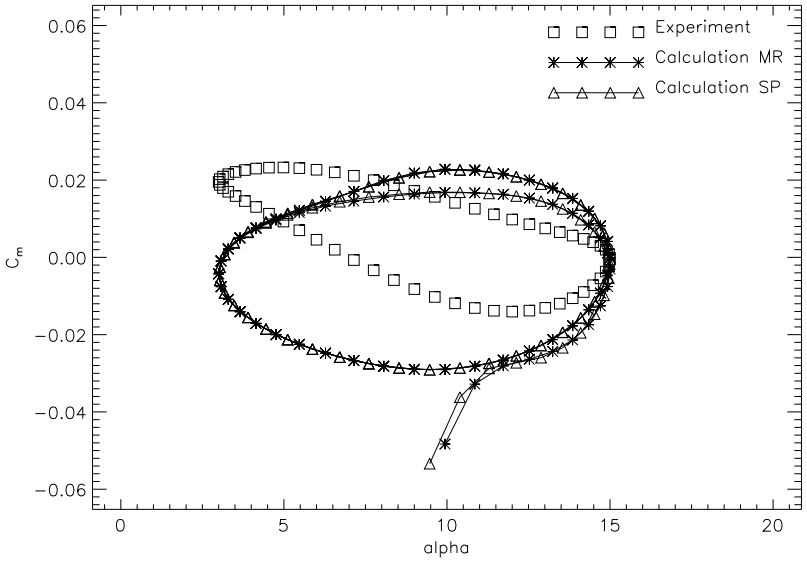

Figure 8: Pitching moment hysteresis curve for delta wing in pitching motion ($\omega = 1.12$, $\bar{\alpha} = 9°$, $\triangle\alpha = 12°$, 3 periods with 40 time steps/period).

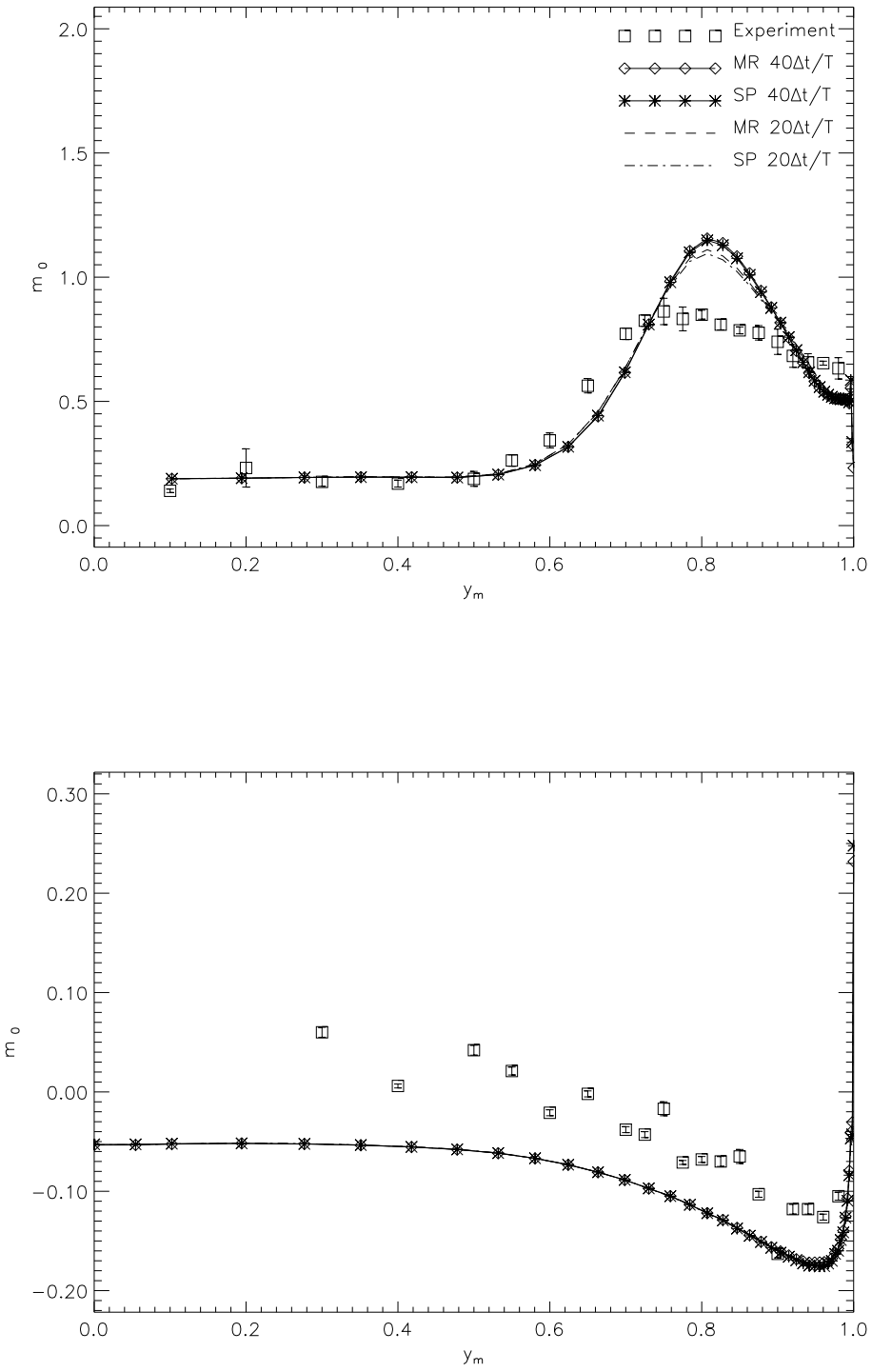

Figure 9: Amplitude m_0 of $-Cp$ on upper and lower wing surface in cross-section at $x_m = 0.6$ of delta wing in pitching motion ($\omega = 1.12$, $\bar{\alpha} = 9°$, $\triangle\alpha = 12°$).

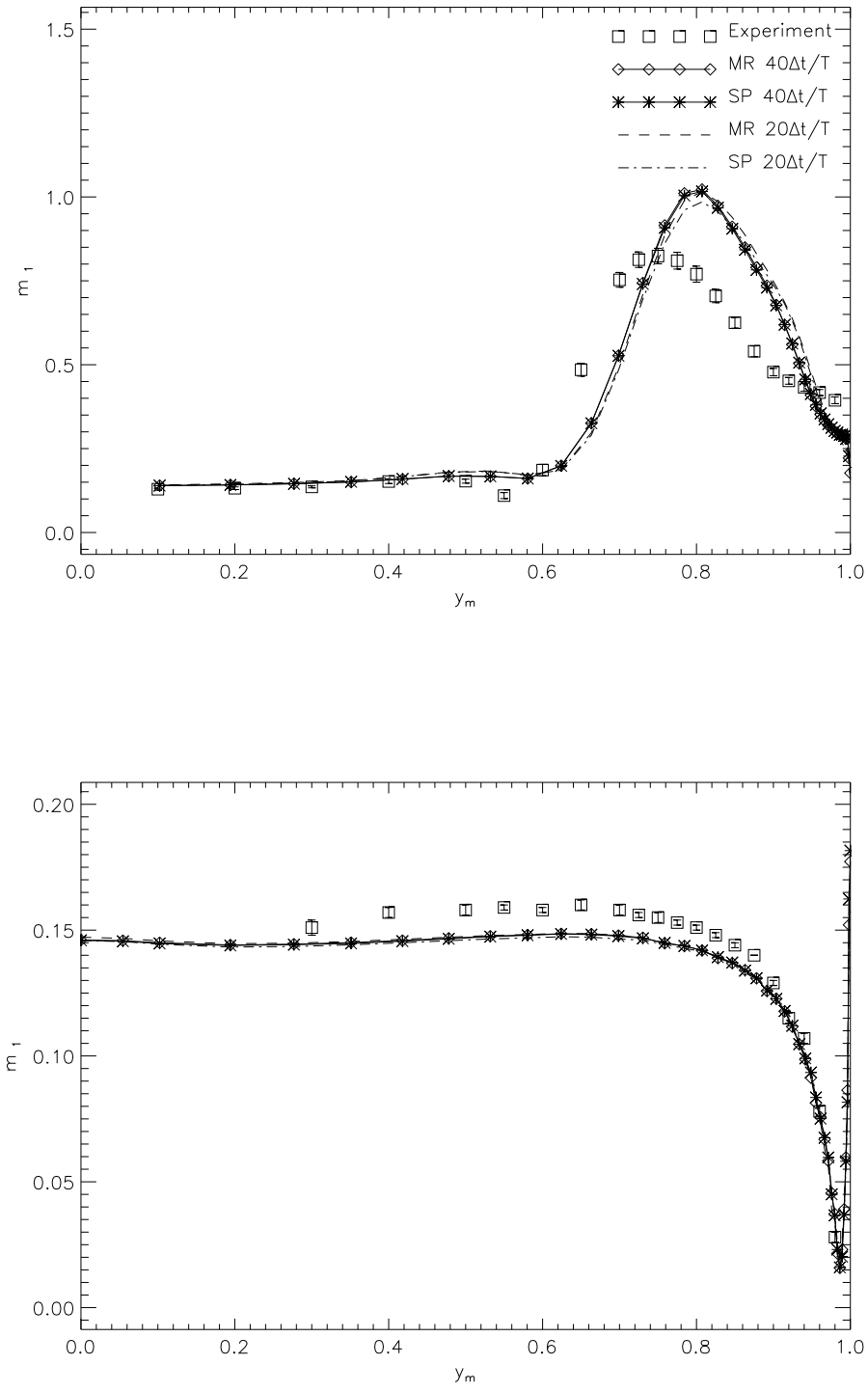

Figure 10: Amplitude m_1 of $-Cp$ on upper and lower wing surface in cross-section at $x_m = 0.6$ of delta wing in pitching motion ($\omega = 1.12$, $\bar{\alpha} = 9°$, $\triangle\alpha = 12°$).

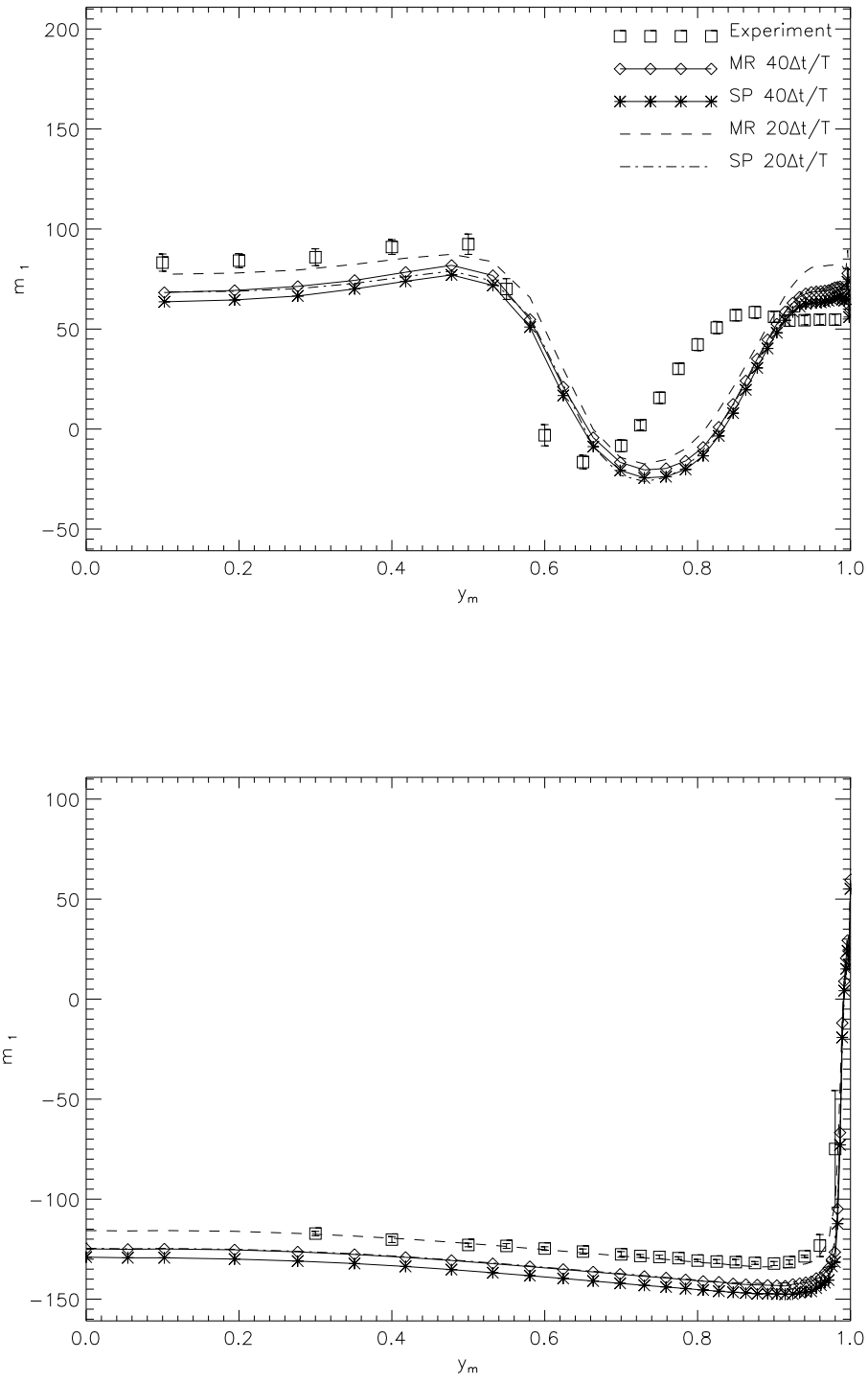

Figure 11: Phase m_1 of $-Cp$ on upper and lower wing surface in cross-section at $x_m = 0.6$ of delta wing in pitching motion ($\omega = 1.12$, $\bar{\alpha} = 9°$, $\triangle\alpha = 12°$).

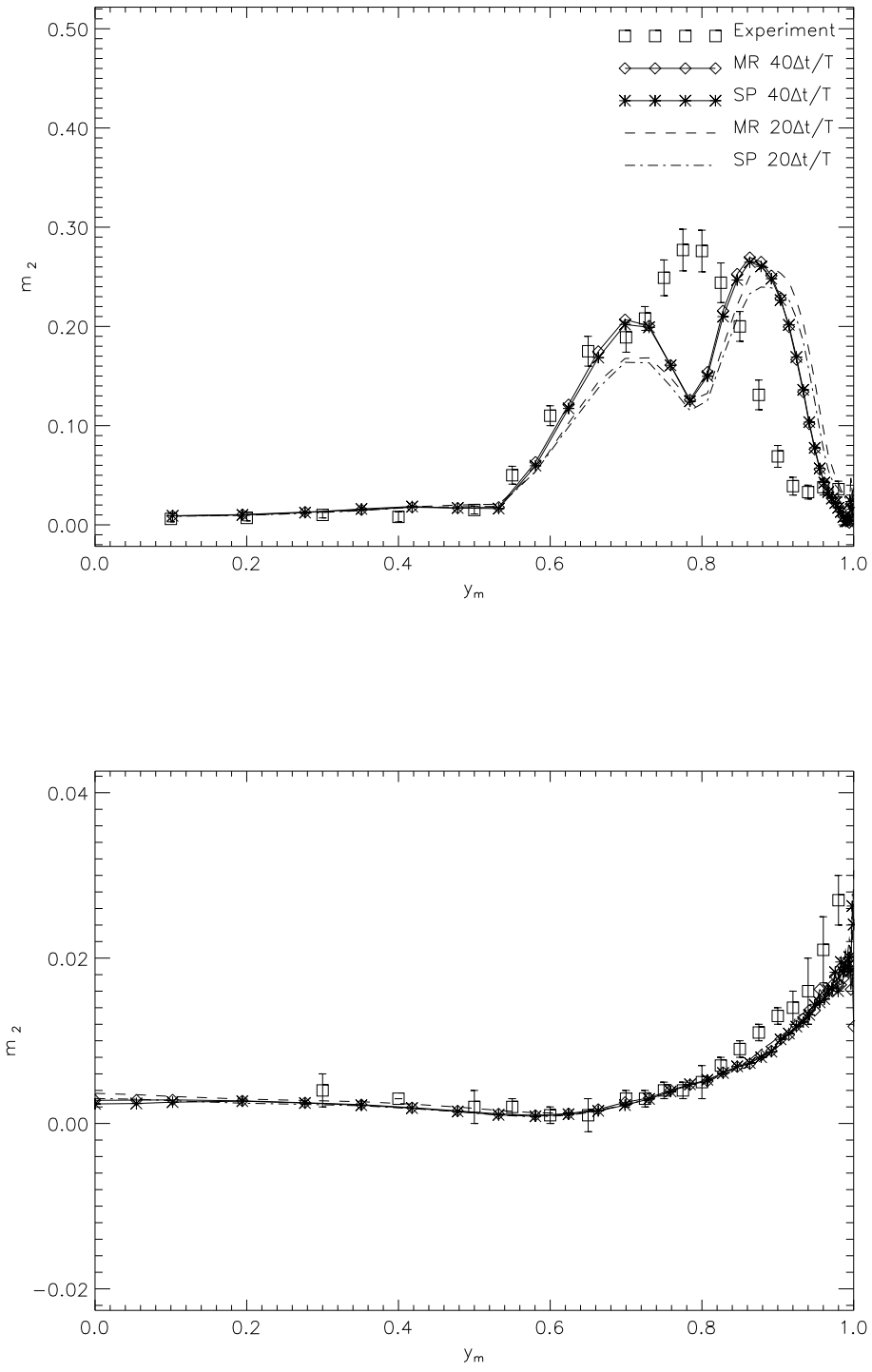

Figure 12: Amplitude m_2 of $-Cp$ on upper and lower wing surface in cross-section at $x_m = 0.6$ of delta wing in pitching motion ($\omega = 1.12$, $\bar{\alpha} = 9°$, $\triangle\alpha = 12°$).

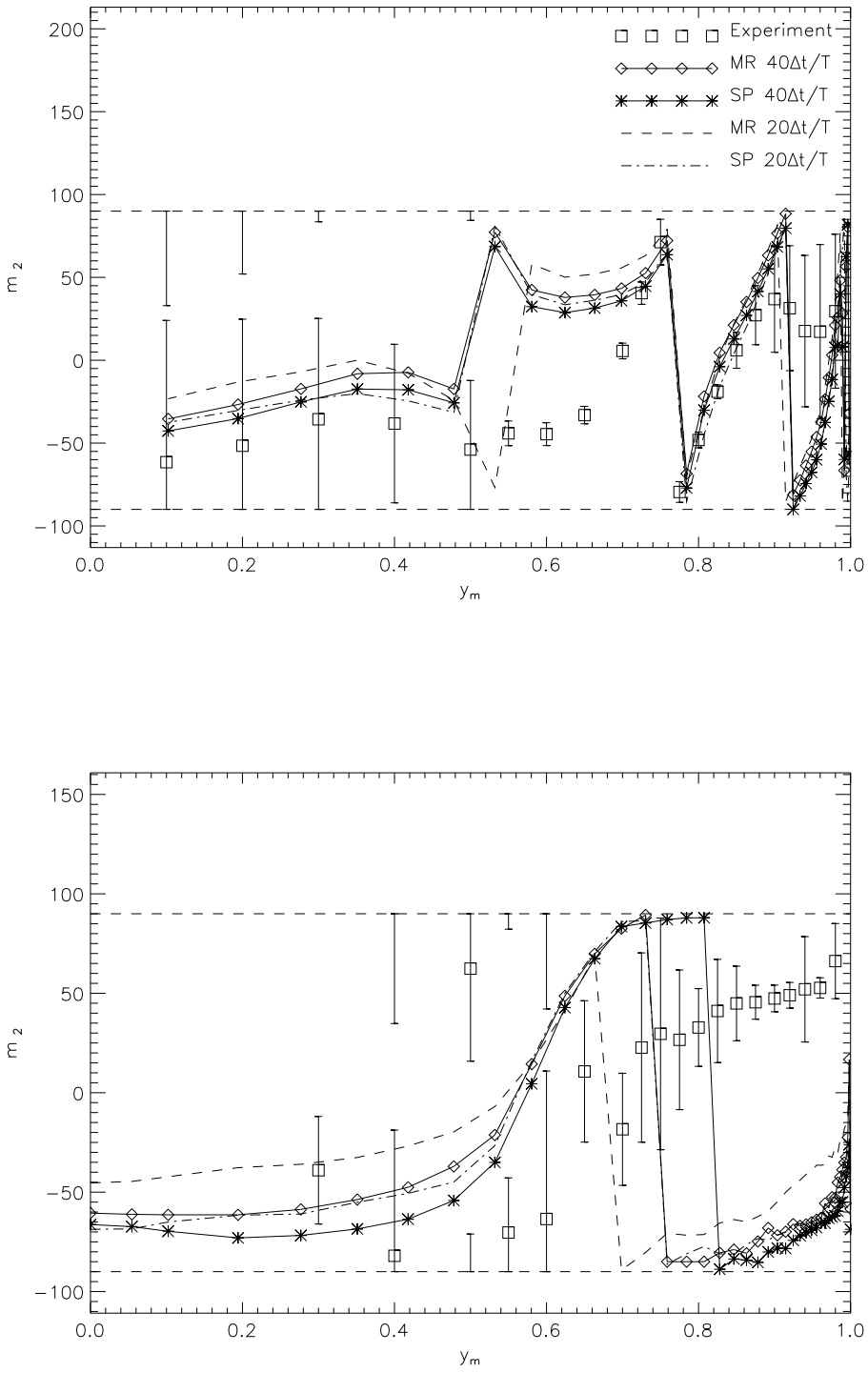

Figure 13: Phase m_2 of $-Cp$, modulo 180°, on upper and lower wing surface in cross-section at $x_m = 0.6$ of delta wing in pitching motion ($\omega = 1.12$, $\bar{\alpha} = 9°$, $\triangle\alpha = 12°$).

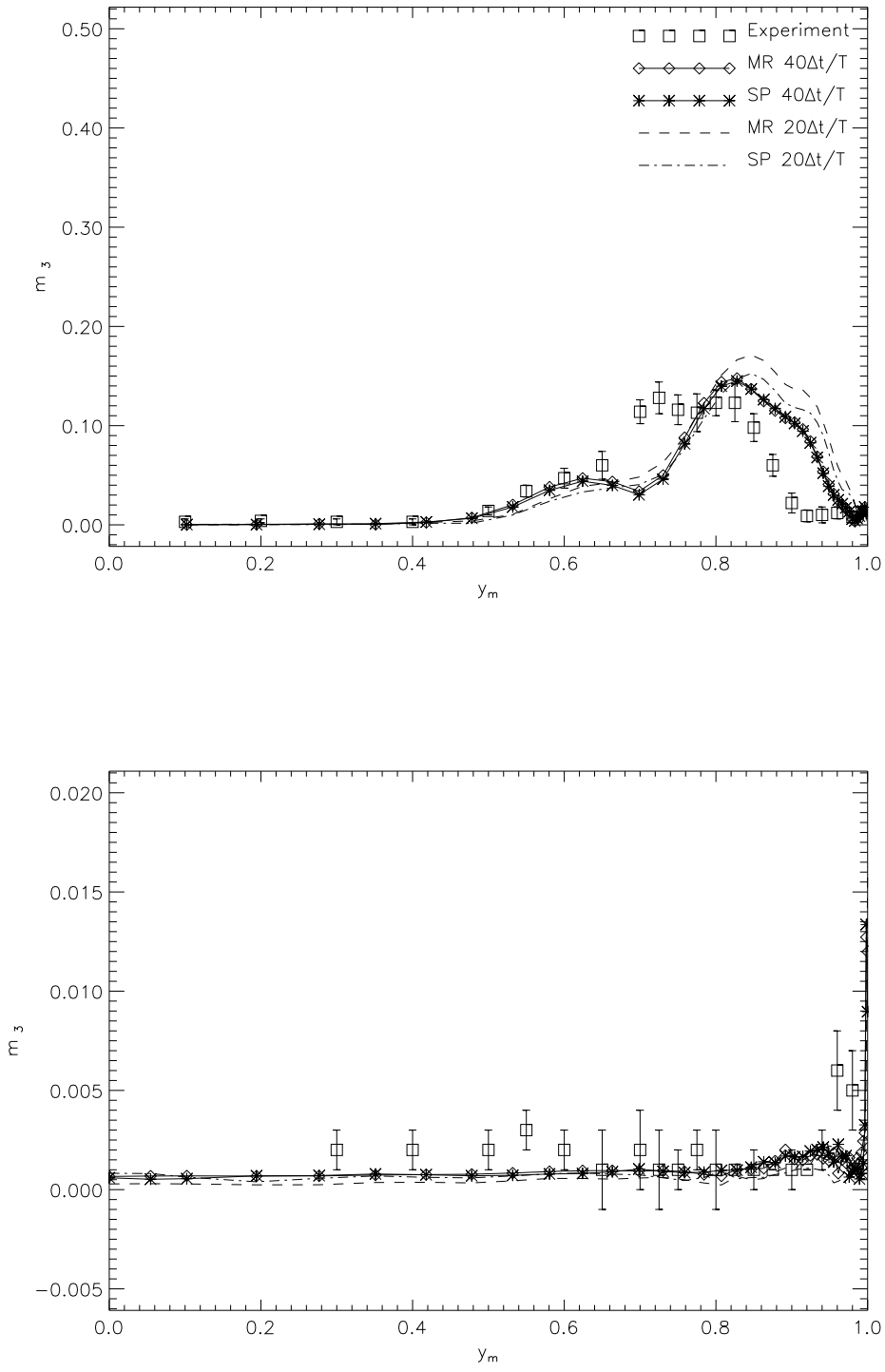

Figure 14: Amplitude m_3 of $-Cp$ on upper and lower wing surface in cross-section at $x_m = 0.6$ of delta wing in pitching motion ($\omega = 1.12$, $\bar{\alpha} = 9°$, $\triangle\alpha = 12°$).

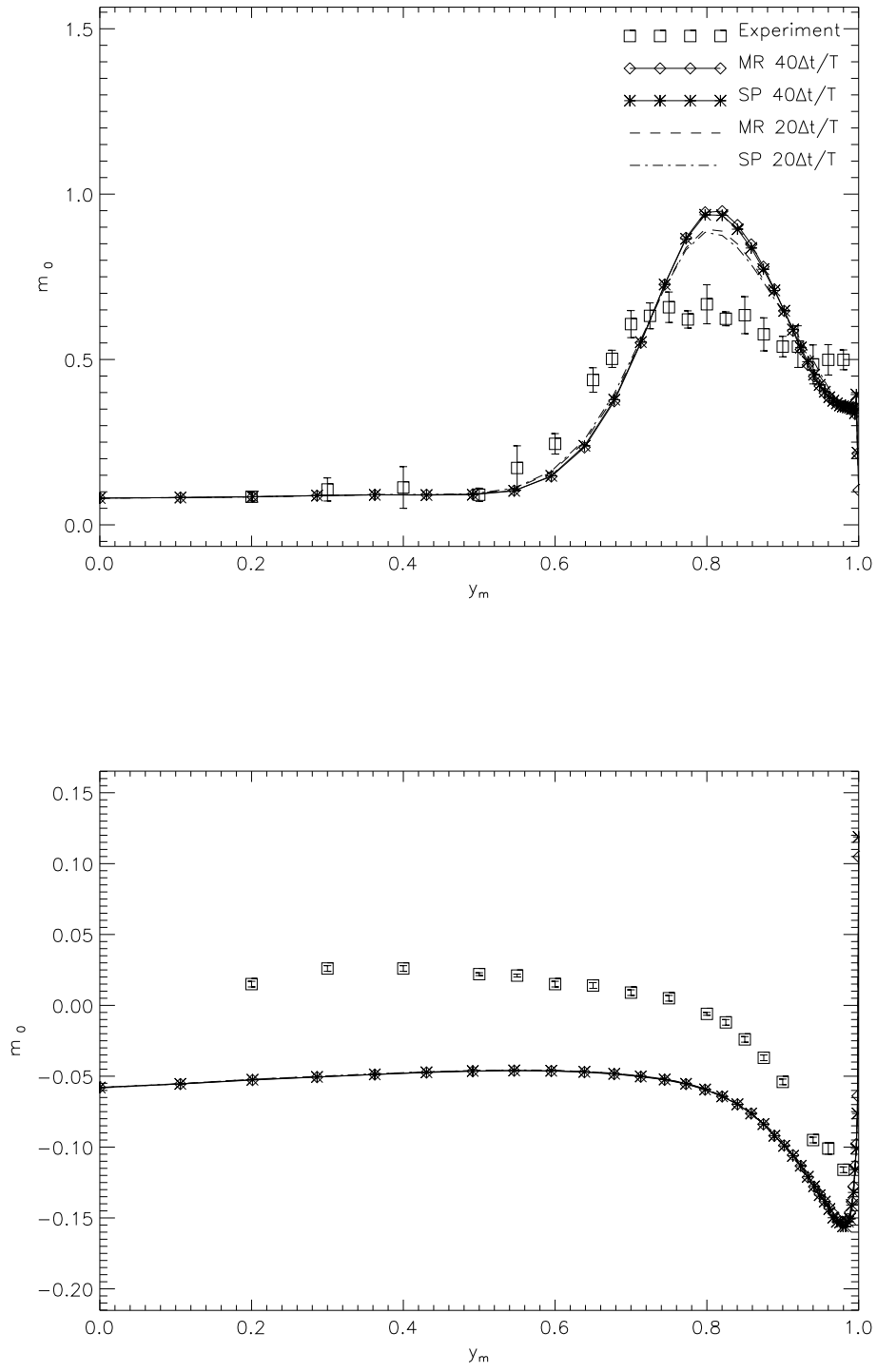

Figure 15: Amplitude m_0 of $-Cp$ on upper and lower wing surface in cross-section at $x_m = 0.8$ of delta wing in pitching motion ($\omega = 1.12$, $\bar{\alpha} = 9°$, $\triangle\alpha = 12°$).

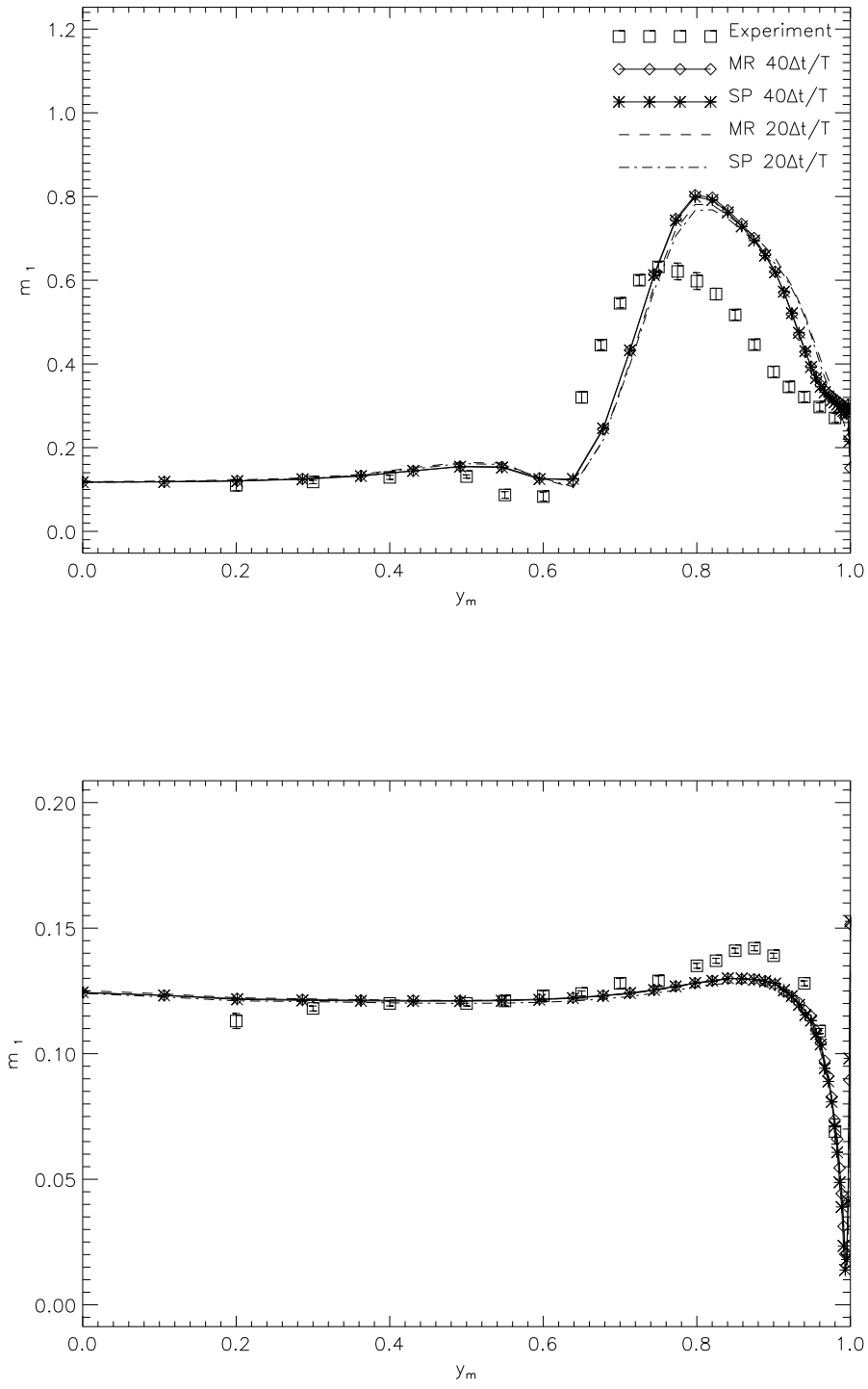

Figure 16: Amplitude m_1 of $-Cp$ on upper and lower wing surface in cross-section at $x_m = 0.8$ of delta wing in pitching motion ($\omega = 1.12$, $\bar{\alpha} = 9°$, $\triangle\alpha = 12°$).

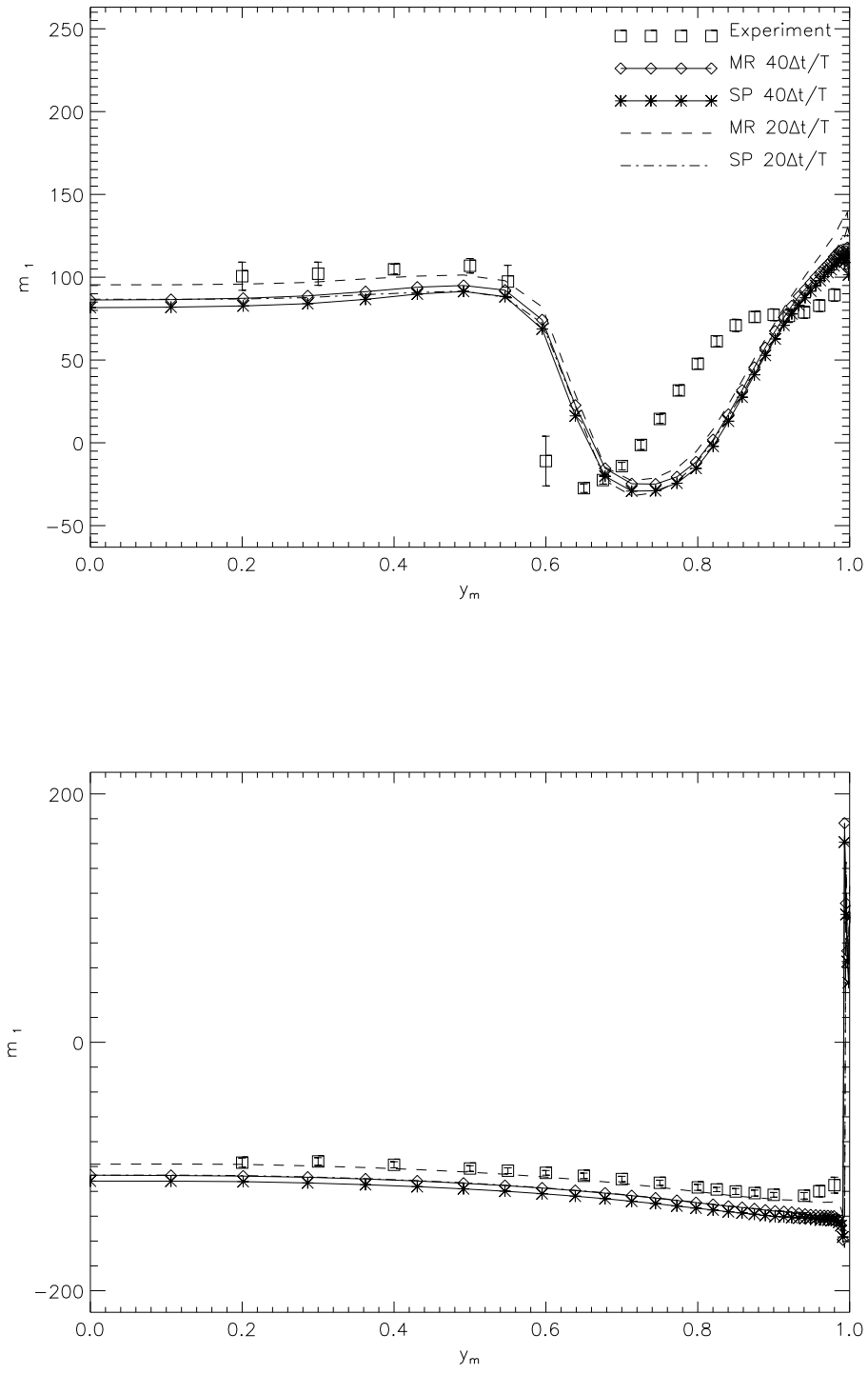

Figure 17: Phase m_1 of $-Cp$ on upper and lower wing surface in cross-section at $x_m = 0.8$ of delta wing in pitching motion ($\omega = 1.12$, $\bar{\alpha} = 9°$, $\triangle\alpha = 12°$).

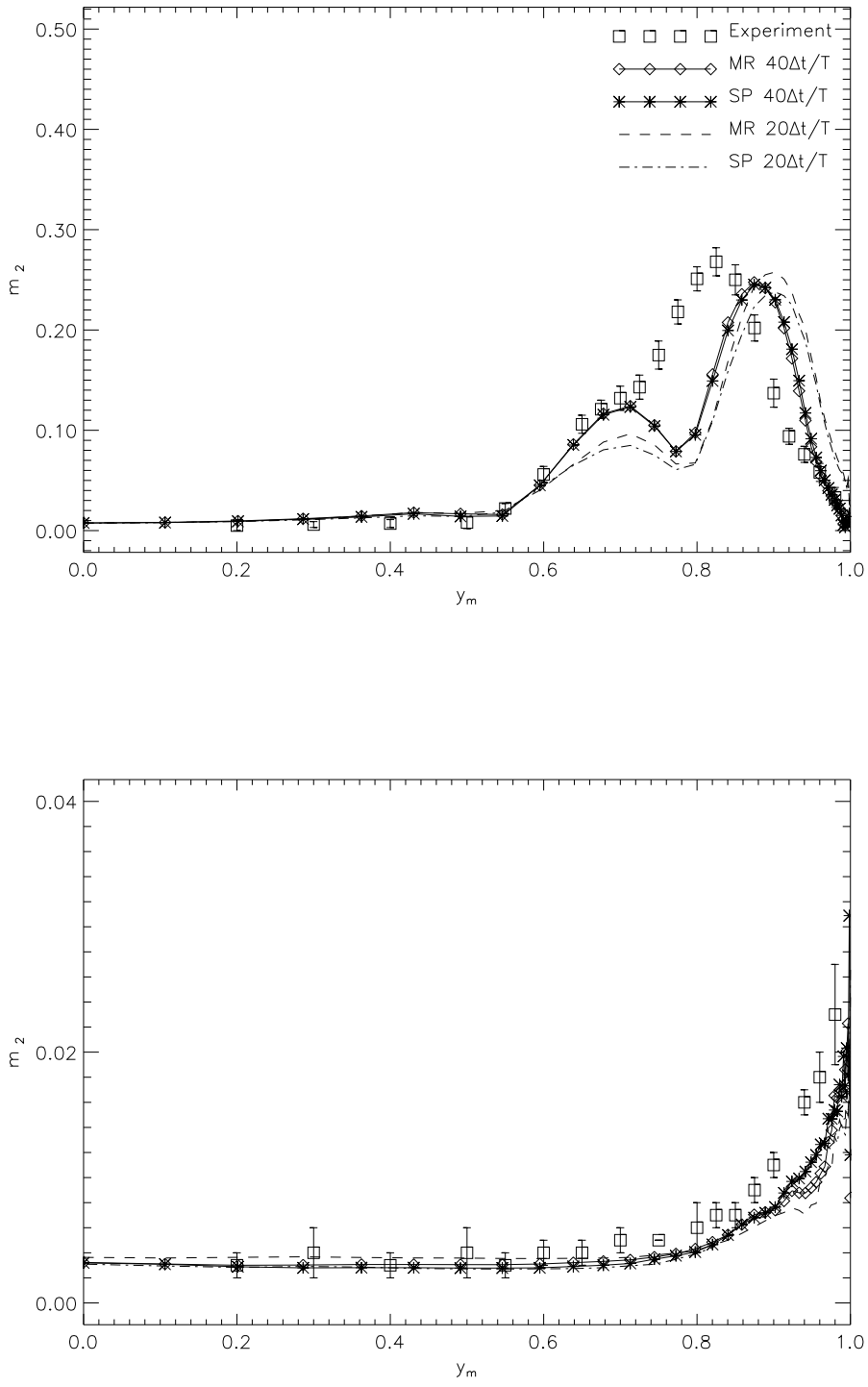

Figure 18: Amplitude m_2 of $-Cp$ on upper and lower wing surface in cross-section at $x_m = 0.8$ of delta wing in pitching motion ($\omega = 1.12$, $\bar{\alpha} = 9°$, $\triangle\alpha = 12°$).

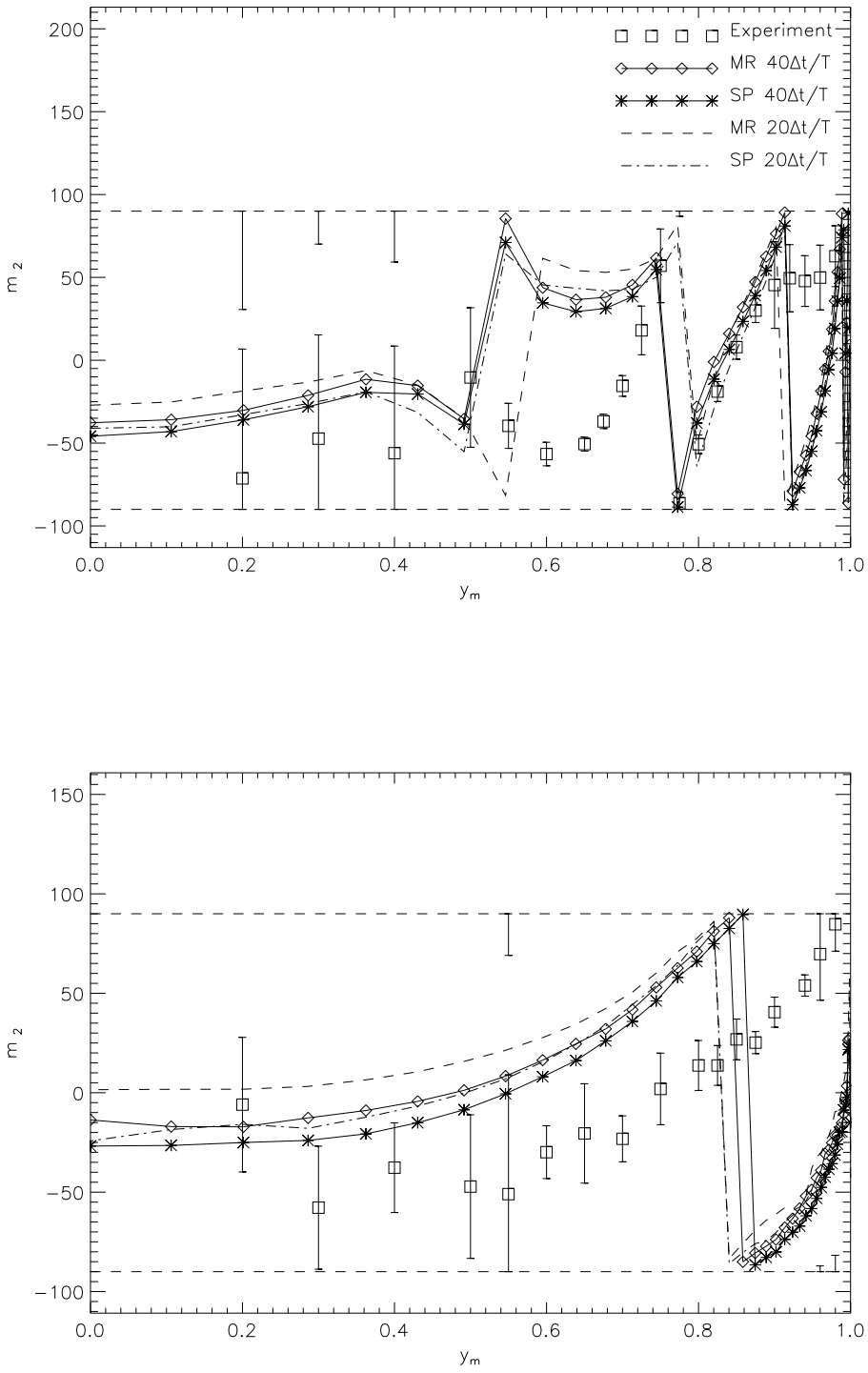

Figure 19: Phase m_2 of $-Cp$, modulo 180°, on upper and lower wing surface in cross-section at $x_m = 0.8$ of delta wing in pitching motion ($\omega = 1.12$, $\bar{\alpha} = 9°$, $\triangle\alpha = 12°$).

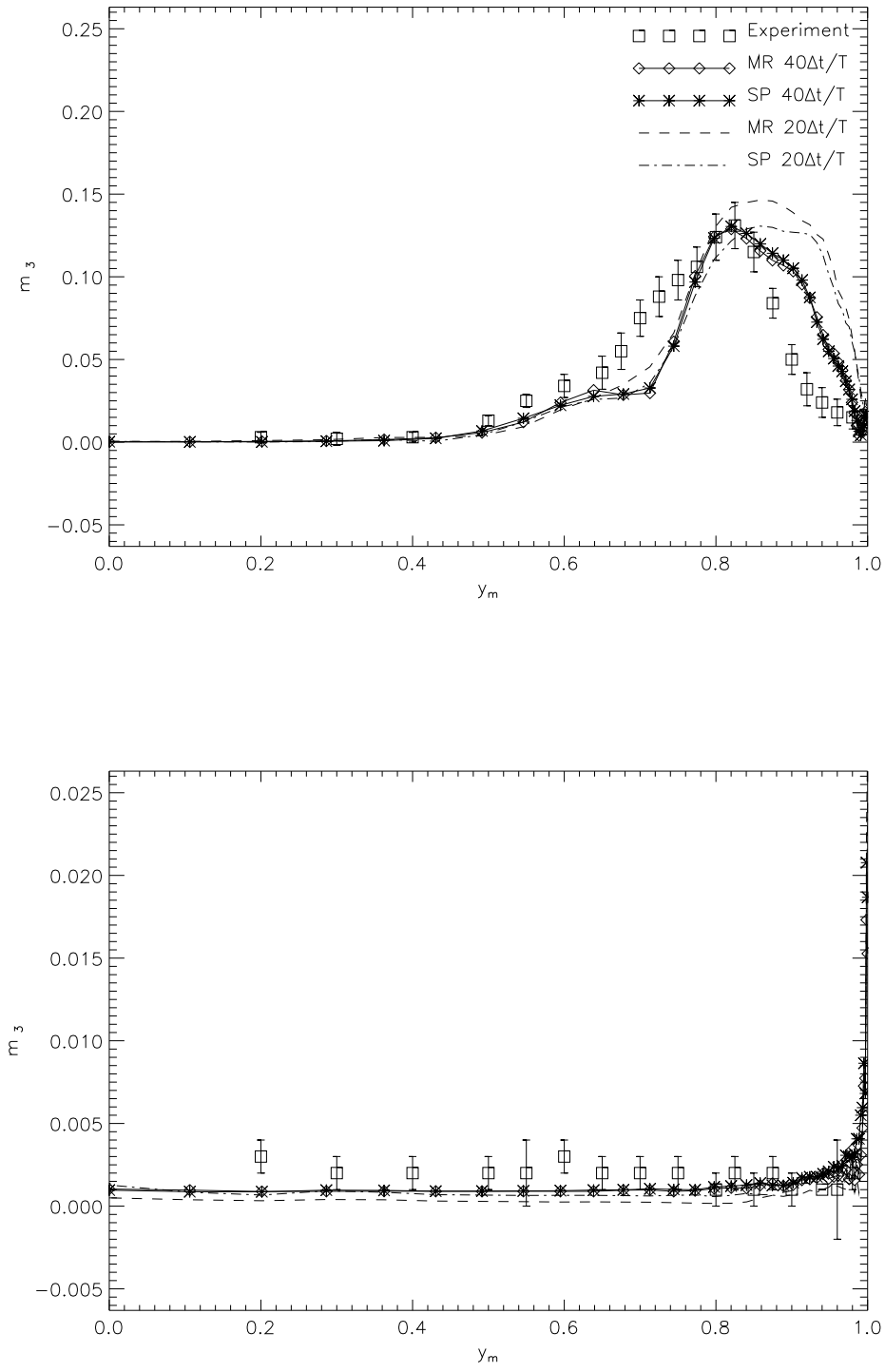

Figure 20: Amplitude m_3 of $-Cp$ on upper and lower wing surface in cross-section at $x_m = 0.8$ of delta wing in pitching motion ($\omega = 1.12$, $\bar{\alpha} = 9°$, $\triangle\alpha = 12°$).